

Manuscript Details

Manuscript number	ATMOSRES_2019_931_R1
Title	Classifying aerosol particles through the combination of optical and physical-chemical properties: Results from a wintertime campaign in Rome (Italy)
Article type	Research Paper

Abstract

The “Carbonaceous Aerosol in Rome and Environs” (CARE) experiment took place at a Mediterranean urban background site in Rome (Italy) deploying a variety of instrumentation to assess aerosol physical-chemical and optical properties with high-time resolution (from 1 minute to 2 hours). In this study, aerosol optical properties, chemical composition, and size distribution data were examined with a focus on the analysis of several intensive optical properties obtained from multi-wavelength measurements of aerosol scattering and absorption coefficients. The spectral behaviour of several quantities related to both aerosol composition and size was explored, analysing their high-time resolved temporal patterns and combining them in order to extract the maximum information from all the available data. A methodology to separate aerosol types using optical data only is here proposed and applied to an urban area characterised by a complex mixture of particles. A key is given to correctly disentangle cases that could not be distinguished observing only one or few parameters, but that can be clearly separated using a suitable ensemble of optical properties. The SSCAAE, i.e. the wavelength dependence of the Single Scattering co-albedo 1-SSA (where SSA is the Single Scattering Albedo) - that efficiently responds to both aerosol size and chemical composition – resulted to be the best optical intensive parameter to look at for the discrimination between episodes characterised by specific aerosol types (e.g. sea salt, Saharan dust) and more mixed conditions dominated by local emissions. However, this study also highlighted that it is necessary to combine temporal patterns of different optical parameters to robustly associate SSCAAE features to specific aerosol types. In addition, the complete chemical speciation and the high-time resolved size distribution were used to confirm the aerosol types identified via a combination of aerosol optical properties. Look-up tables with most suitable ranges of values for optical variables were produced; therefore, these pieces of information can be used at the same site or at locations with similar features to quickly identify the occurrence of aerosol episodes. Graphical frameworks (both from the literature and newly designed) are also proposed; for each scheme features, advantages, and limitations are discussed.

Keywords	Intensive optical properties, high time resolution, aerosol classification schemes
Manuscript category	Aerosol particles
Corresponding Author	Roberta Vecchi
Corresponding Author's Institution	Dept. of Physics Università degli Studi di Milano
Order of Authors	Sara Valentini, Francesca Barnaba, Vera Bernardoni, Giulia Calzolai, Francesca Costabile, Luca Di Liberto, Alice Forello, Gian Paolo Gobbi, Maurizio Gualtieri, Franco Lucarelli, Silvia Nava, Ettore Petralia, Gianluigi Valli, Alfred Wiedensohler, Roberta Vecchi
Suggested reviewers	Martine Collaud Coen, Daniele Contini, Hans Moosmuller, Helmut Horvath, M. Pandolfi

Submission Files Included in this PDF

File Name [File Type]

Response to Reviewers.docx [Response to Reviewers]

Highlights_REV.docx [Highlights]

Paper_Valentini_final-REV.docx [Manuscript File]

declaration-of-competing-interests.docx [Conflict of Interest]

SUPPLEMENTARY_Valentini_final-REV.docx [Supplementary Material]

To view all the submission files, including those not included in the PDF, click on the manuscript title on your EVISE Homepage, then click 'Download zip file'.

Research Data Related to this Submission

There are no linked research data sets for this submission. The following reason is given:
Data will be made available on request

Highlights

- Combination of intensive optical parameters discriminates aerosol types.
- High-time resolved composition and size distribution support the identification
- The methodology produces look-up tables useful for real-time implementation.
- High PM events origin can be identified by optical parameters only.

1
2
3
4 1 **Classifying aerosol particles through the combination of optical and physical-chemical properties:**
5 2 **Results from a wintertime campaign in Rome (Italy)**

6
7 3 Valentini S.¹, Barnaba F.², Bernardoni V.¹, Calzolari G.³, Costabile F.², Di Liberto L.², Forello A.C.¹,
8 4 Gobbi G.P.², Gualtieri M.⁴, Lucarelli F.^{3,5}, Nava S.^{3,5}, Petralia E.⁴, Valli G.¹, Wiedensohler A.⁶, Vecchi
9 5 R.^{1,*}

10
11
12 6 ¹Department of Physics, Università degli Studi di Milano and INFN-Milan, 20133 Milan, Italy

13 7 ²CNR Institute of Atmospheric Sciences and Climate, Via Fosso del Cavaliere 100, 00133 Rome, Italy

14 8 ³INFN-Florence, 50019 Sesto Fiorentino, Italy

15 9 ⁴ENEA – SSPT – MET – Atmospheric Pollution Laboratory (INAT), via Martiri di Monte Sole 4, 40129
16 10 Bologna, Italy

17 11 ⁵Department of Physics and Astronomy, Università degli Studi di Firenze, 50121 Florence, Italy

18 12 ⁶Leibniz Institute for Tropospheric Research, Permoserstrasse 15, 04318 Leipzig, Germany;

19 13 *corresponding author: Roberta Vecchi – roberta.vecchi@unimi.it
20 14

21
22
23 15 **Abstract**

24 16 The “Carbonaceous Aerosol in Rome and Environs” (CARE) experiment took place at a
25 17 Mediterranean urban background site in Rome (Italy) deploying a variety of instrumentation to
26 18 assess aerosol physical-chemical and optical properties with high-time resolution (from 1 minute to
27 19 2 hours). In this study, aerosol optical properties, chemical composition, and size distribution data
28 20 were examined with a focus on the analysis of several intensive optical properties obtained from
29 21 multi-wavelength measurements of aerosol scattering and absorption coefficients. The spectral
30 22 behaviour of several quantities related to both aerosol composition and size was explored, analysing
31 23 their high-time resolved temporal patterns and combining them in order to extract the maximum
32 24 information from all the available data.

33 25 A methodology to separate aerosol types using optical data only is here proposed and applied to an
34 26 urban area characterised by a complex mixture of particles. A key is given to correctly disentangle
35 27 cases that could not be distinguished observing only one or few parameters, but that can be clearly
36 28 separated using a suitable ensemble of optical properties.

37 29 The SSCAAE, i.e. the wavelength dependence of the Single Scattering co-albedo 1-SSA (where SSA is
38 30 the Single Scattering Albedo) - that efficiently responds to both aerosol size and chemical
39 55

60
61
62 31 composition – resulted to be the best optical intensive parameter to look at for the discrimination
63
64 32 between episodes characterised by specific aerosol types (e.g. sea salt, Saharan dust) and more
65
66 33 mixed conditions dominated by local emissions. However, this study also highlighted that it is
67
68 34 necessary to combine temporal patterns of different optical parameters to robustly associate
69
70 35 SSCAAE features to specific aerosol types. In addition, the complete chemical speciation and the
71
72 36 high-time resolved size distribution were used to confirm the aerosol types identified via a
73
74 37 combination of aerosol optical properties. Look-up tables with most suitable ranges of values for
75
76 38 optical variables were produced; therefore, these pieces of information can be used at the same
77
78 39 site or at locations with similar features to quickly identify the occurrence of aerosol episodes.
79
80 40 Graphical frameworks (both from the literature and newly designed) are also proposed; for each
81
82 41 scheme features, advantages, and limitations are discussed.
83

84 42
85
86 43 Keywords: Intensive optical properties, high time resolution, aerosol classification schemes.
87

88 44 89 45 **1. Introduction**

90 46 Atmospheric aerosol is a complex mixture of suspended particles characterized by a huge variability
91
92 47 in terms of chemical composition, size and shape. Aerosols can have a direct (by direct scattering
93
94 48 and absorption) and indirect (by impacting on cloud formation and albedo) effect on atmospheric
95
96 49 radiation (IPCC, 2013). Moreover, atmospheric aerosol is known to have detrimental effects on
97
98 50 human health (Dockery et al., 1993; Pope et al., 2002).

99 51 Estimates of the climate impacts of atmospheric aerosol and their optical properties are affected by
100
101 52 very large uncertainties; nevertheless, direct measurements of aerosol optical properties are not
102
103 53 usually performed by air quality (AQ) monitoring networks, in contrast to particle concentration and
104
105 54 chemical composition, often performed for different size fractions. Aerosol optical properties are
106
107 55 related to the size and composition of the particles, as well as to their mixing state (e.g. Bond and
108
109 56 Bergstrom, 2006). Spectral scattering and absorption properties depend on the considered aerosol
110
111 57 type; therefore, simultaneous measurements of multi-wavelength aerosol optical properties,
112
113 58 chemical composition, and size distribution can improve our knowledge about atmospheric particles
114
115 59 impact on the radiative forcing and air quality.

116 60 Several classification schemes have been proposed in the literature to distinguish aerosol types and
117
118 61 mixtures. Most of these methods make use of column-integrated properties usually retrieved from

119
120
121
122
123
124
125
126
127
128
129
130
131
132
133
134
135
136
137
138
139
140
141
142
143
144
145
146
147
148
149
150
151
152
153
154
155
156
157
158
159
160
161
162
163
164
165
166
167
168
169
170
171
172
173
174
175
176
177

62 remote-sensing data, such as those provided by the global network of ground-based sun and sky
63 radiometers AERONET (Aerosol Robotic Network) or obtained by Sun photometers (e.g. Dubovik et
64 al., 2002; Gobbi et al., 2007; Kalapureddy et al., 2009; Russell et al., 2010; Giles et al., 2011, 2012;
65 Cazorla et al., 2013, Rupakheti et al., 2019). There are also few studies dealing with in-situ
66 measurements of optical properties, both ground-based and airborne (e.g. Yang et al., 2009; Lee et
67 al., 2012; Costabile et al., 2013; Cappa et al., 2016, Donato et al., 2018, Romano et al., 2019). As
68 pointed out by Schmeisser et al. (2017), the majority of the existing classification schemes work well
69 at sites where the aerosol characteristics are fairly homogeneous, while their performance is worse
70 in areas that experience a heterogeneity of particle sources and/or episodes characterised by
71 aerosol transported from e.g. deserts or oceans. The methods proposed to distinguish PM types are
72 sometimes supported by chemical composition, size distribution data, or back trajectory analyses;
73 however, these pieces of information are not usually included in the classifying approaches
74 themselves.

75 Data analysed in this paper were collected in the frame of the CARE Experiment (Carbonaceous
76 Aerosol in Rome and Environs), which was carried out in Rome (Italy) using a variety of instruments
77 and techniques to obtain a comprehensive and highly time-resolved picture of the aerosol
78 properties at a Mediterranean urban background site. Indeed, several studies in recent literature
79 (e.g. Timonen et al., 2010; Lucarelli et al., 2015; Costabile et al., 2017) pointed out the importance
80 of shorter time scale (<1h) to study atmospheric processes and source variability. The CARE
81 campaign was carried out at a site impacted by different local emission sources and sometimes
82 affected by medium-long range transport of e.g. sea salt or Saharan dust. An overview of
83 measurements performed and methodologies applied during the CARE experiment is given by
84 Costabile et al. (2017).

85 A phenomenology of specific episodes characterised by aerosol with different properties is given
86 exploiting all the available information about high-time resolved optical properties, chemical
87 composition, and size distribution of atmospheric aerosol. The main objective here is to find out one
88 or more possible combinations of intensive optical parameters that can be used as a tool to identify
89 aerosols with different origin. In addition, graphical classification schemes reported in the literature
90 were applied and some were newly developed to visually distinguish specific episodes and aerosol
91 types via 2D plots of optical parameters. These representations appear useful to have a first hint on
92 the typologies of particles observed during a campaign, even though they are not able to clearly

178
179
180
181
182
183
184
185
186
187
188
189
190
191
192
193
194
195
196
197
198
199
200
201
202
203
204
205
206
207
208
209
210
211
212
213
214
215
216
217
218
219
220
221
222
223
224
225
226
227
228
229
230
231
232
233
234
235
236

93 disentangle different contributions, especially when atmospheric aerosol is dominated by mixtures
94 of particles emitted by a variety of sources. In these cases, it is shown here that, exploiting multi-
95 wavelength optical properties measured with high-time resolution, only the combined analysis of
96 their temporal patterns allows to identify the dominant contributions.

2. Material and Methods

2.1 Site description

The CARE experiment took place from January 27th to February 28th 2017 at an urban background site in downtown Rome. Due to its geographical position (in the middle of the Mediterranean Sea) and its meteorological conditions, this site can experience the advection of air masses transported from the Sahara Desert (Barnaba and Gobbi, 2004; Gobbi et al., 2007; Barnaba et al., 2017; Gobbi et al., 2019) or from the sea (Perrino et al., 2009). The CARE measurement site is also affected by local urban sources such as vehicular traffic and biomass burning for heating and cooking (Costabile et al., 2017 and 2019).

2.2 Aerosol characterisation techniques

A detailed list of the instruments deployed during the CARE experiment and their operating conditions has been already reported in Costabile et al. (2017). Instruments and techniques which produced data here analysed will be shortly described in the following. Where not specified, instruments were operated at ambient relative humidity (RH).

2.2.1 Wavelength-dependent optical properties

On-line instruments continuously measured multi-wavelength PM₁₀ scattering and absorption coefficients with a time resolution of 1 minute. In this study, 5-minute averages of each parameter are considered in order to reduce data noise.

A 3-wavelength integrating Nephelometer (Aurora 3000, Ecotech) measured dry aerosol scattering coefficient $\sigma_s(\lambda)$ at 450, 525, and 635 nm. Total scattering coefficients were corrected for truncation error according to Müller et al. (2011a).

On-line dry aerosol absorption coefficient $\sigma_a(\lambda)$ at 7 wavelengths (370, 470, 520, 590, 660, 880, and 950 nm) was retrieved by equivalent Black Carbon (eBC) concentrations measured by a dual-spot

237

238

239

240

241

242

243

244

245

246

247

248

249

250

251

252

253

254

255

256

257

258

259

260

261

262

263

264

265

266

267

268

269

270

271

272

273

274

275

276

277

278

279

280

281

282

283

284

285

286

287

288

289

290

291

292

293

294

295

124 Aethalometer (AE33, Magee Scientific) (Drinovec et al., 2015) and using instrument-specific Mass
125 Absorption Cross sections (MAC) at different wavelengths.

126 Moreover, a Multi-Angle Absorption Photometer (MAAP, Thermo Scientific) was used to measure
127 eBC concentration at RH<30%. From these data, $\sigma_a(637)$ was retrieved using the MAC of 6.6 m²/g
128 set in the MAAP and a wavelength correction factor of 1.05 as reported in Müller et al. (2011b).

2.2.2 Chemical analyses

131 Both on-line and off-line techniques were used to assess aerosol chemical composition (elements,
132 carbonaceous fractions, non-refractory components) on different size fractions with time resolution
133 from 30 minutes to 2 hours.

134 PM2.5 samples collected with 1-hour time resolution using a streaker sampler were analysed off-
135 line as for elemental composition by Particle Induced X-Ray Emission (PIXE) analysis (Calzolari et al.,
136 2015). This technique allows the detection and quantification of Z>10 elements.

137 A Sunset Field Thermal-Optical Analyser (Model-4 Semi-Continuous OC-EC Field Analyzer – Sunset
138 Laboratory inc.) measured elemental carbon (EC) and organic carbon (OC) in PM2.5 with a 2-hour
139 time resolution.

140 An Aerodyne Aerosol Chemical Speciation Monitor (ACSM; Ng et al., 2011) provided PM1 non-
141 refractory chemical components (organic matter, sulphate, ammonium, nitrate, and chloride ions)
142 on-line. The instrument operated at RH<30% with 30-minute time resolution and 1-hour averages
143 were then calculated. Organic aerosol (OA) concentration apportioned among the sources by the
144 SoFi software (Canonaco et al., 2013) was also analysed as an additional information; vehicular
145 traffic (HOA), oxygenated secondary aerosol (OOA), and biomass burning (BBOA) were the major
146 components taken into account.

2.2.3 Particle number size distributions

147 To obtain particle number size distribution (PNSD), a Scanning Mobility Particle Sizer (TROPOS-
148 SMPS) and an Aerodynamic Particle Sizer (APS, TSI) were employed during the CARE campaign. Both
149 instruments were operated with a time resolution of 5 minutes. SMPS and APS covered the 8-700
150 nm range in electrical mobility diameter (d_m) and 0.5-20 μ m in aerodynamic diameter (d_a),
151 respectively. To obtain a unique number size distribution in the range $8 \text{ nm} \leq d_m \leq 10 \mu\text{m}$, APS data
152 were converted to a d_m -based size distribution (i.e. $dN/d\log(d_m)$) and then merged to SMPS output

296
297
298
299
300
301
302
303
304
305
306
307
308
309
310
311
312
313
314
315
316
317
318
319
320
321
322
323
324
325
326
327
328
329
330
331
332
333
334
335
336
337
338
339
340
341
342
343
344
345
346
347
348
349
350
351
352
353
354

155 following the procedure described in Khlystov et al. (2004). More details about the PNSD calculation
156 at the CARE site can be found in Costabile et al. (2017) and in Alas et al. (2019).

158 3. Calculations

159 3.1 Aethalometer data corrections

160 The multi-wavelength aerosol absorption coefficient $\sigma_a(\lambda)$ was obtained by an AE33 Aethalometer,
161 which gives eBC concentration using instrument-specific MAC values at seven wavelengths (e.g.
162 10.35 m²/g at 660 nm). As described in Drinovec et al. (2015), the instrument internal software
163 retrieves $\sigma_a(\lambda)$ from attenuation measurements and corrects them for loading (k parameter) and
164 multiple scattering (C factor) effects. It is noteworthy that literature studies (e.g. Collaud Coen et
165 al., 2010; Segura et al., 2014) pointed out the site-specificity and possible wavelength dependence
166 of these effects.

167 As evidenced by some recent literature studies (e.g. Goetz et al., 2018), the C factor equal to 1.57
168 currently fixed in AE33 to convert attenuation into absorption can lead to a significant
169 overestimation of the $\sigma_a(\lambda)$ by this instrument. Aiming at reducing this bias, in this work the
170 availability of parallel (independent) optical measurements was exploited and - following Collaud
171 Coen et al. (2010) -the loading-corrected C factor (here C_{corr}) was inferred via a linear regression
172 analysis between the attenuation coefficient (loading-corrected) $\sigma_{atn,k}(660)$ calculated from the eBC
173 concentration given by the AE33 and $\sigma_a(637)$ measured by the MAAP. Indeed, the MAAP is often
174 considered as the reference instrument for filter-based measurements of aerosol light absorption
175 coefficient (Müller et al., 2011b), and no simultaneous in-situ σ_a data were available for the CARE
176 campaign. However, Hyvärinen et al. (2013) showed that when eBC concentration is high, the MAAP
177 response lacks in linearity; in this study a non-linear behaviour at $\sigma_a(637) > 100 \text{ Mm}^{-1}$ was observed,
178 thus only MAAP data giving $\sigma_a(637) < 100 \text{ Mm}^{-1}$ were considered in the regression $\sigma_{atn,k}(660)$ vs
179 $\sigma_a(637)$.

180 The AE33 attenuation coefficient $\sigma_{atn,k}(660)$ was retrieved as follows:

$$181 \sigma_{atn,k}(660) = \sigma_a(660) \cdot C = [\text{eBC}(660)] \cdot \text{MAC}_{\text{AE33}}(660) \cdot C = [\text{eBC}(660)] \cdot 10.35 \cdot 1.57$$

182 The linear fit (performed with a Deming regression - see Figure S1) had intercept compatible with
183 zero (within 95% confidence interval) and a slope (i.e. the C_{corr}) of 2.66 that was used to correct the
184 AE33 absorption coefficients at all wavelengths, following the approach developed by Collaud Coen

355

356

357

358

359

360

361

362

363

364

365

366

367

368

369

370

371

372

373

374

375

376

377

378

379

380

381

382

383

384

385

386

387

388

389

390

391

392

393

394

395

396

397

398

399

400

401

402

403

404

405

406

407

408

409

410

411

412

413

185 et al. (2010) and neglecting the possible wavelength-dependence as controversial results are
186 reported in the literature so far.

187 The corrected $\sigma_a(\lambda)$ from AE33 data were then calculated as:

$$188 \sigma_{a,corr}(\lambda) = \sigma_a(\lambda) \cdot C / C_{corr} = \sigma_a(\lambda) \cdot 1.57 / 2.66$$

189 For the sake of simplicity, $\sigma_{a,corr}(\lambda)$ calculated with this procedure will be referred to as $\sigma_a(\lambda)$ in the
190 following.

192 3.2 Intensive optical parameters

193 Wavelength dependences of scattering and absorption coefficients, represented respectively by
194 Scattering Ångström Exponent (SAE) and Absorption Ångström Exponent (AAE), have been used in
195 literature (e.g. Cazorla et al., 2013; Cappa et al., 2016) to distinguish different aerosol types. Indeed,
196 while SAE is mainly related to particle size, AAE is more linked to aerosol composition, even though
197 it is influenced by particle size distribution as well. Consequently, the combination of these two
198 parameters (SAE and AAE) can provide information about the origin and properties of the studied
199 aerosol.

200 In order to highlight possible stronger or weaker dependences of optical properties in some spectral
201 regions, SAE and AAE were here calculated at different wavelength pairs. $SAE(\lambda_1, \lambda_2)$ and $AAE(\lambda_1, \lambda_2)$
202 were thus obtained as

$$203 SAE(\lambda_1, \lambda_2) = - \frac{\ln(\sigma_s(\lambda_1) / \sigma_s(\lambda_2))}{\ln(\lambda_1 / \lambda_2)}$$

$$204 AAE(\lambda_1, \lambda_2) = - \frac{\ln(\sigma_a(\lambda_1) / \sigma_a(\lambda_2))}{\ln(\lambda_1 / \lambda_2)}$$

205 where $\lambda_1 < \lambda_2$

206 With a similar equation Extinction Ångström Exponent $EAE(\lambda_1, \lambda_2)$ was also inferred from extinction
207 coefficients $\sigma_e(\lambda)$ calculated at Nephelometer wavelengths (i.e. 450, 525, and 635 nm) as $\sigma_e(\lambda) =$
208 $\sigma_a(\lambda) + \sigma_s(\lambda)$.

209 Due to the difference in the operating wavelengths of instrumentation used for measurements of
210 scattering and absorption properties, $\sigma_a(\lambda)$ was reported to 450, 525, and 635 nm (i.e. the three
211 operating λ s of the Nephelometer). Since the absorption coefficient wavelength dependence can be
212 represented by a power law ($\sigma_a(\lambda) \sim \lambda^{-AAE}$) with good approximation, the quantity $AAE(\text{fit})$ was
213 calculated via a power-law fit of all 7- λ $\sigma_a(\lambda)$ to exploit all the available absorption spectral range.

For each of the three operating λ s of the Nephelometer, the resulting $\sigma_a(\lambda)$ was then obtained as $\sigma_a(\lambda) = \sigma_a(\lambda_{\text{ref}}) \left(\frac{\lambda}{\lambda_{\text{ref}}} \right)^{-\text{AAE}(\text{fit})}$, where λ_{ref} is the nearest wavelength at which absorption data were available (i.e. 470, 520, and 660 nm for the AE33).

To better analyse the spectral behaviour of $\sigma_a(\lambda)$, the variation in AAE calculated employing different wavelength pairs was considered as the AAE itself may vary with the wavelength (Eck et al., 1999; Schuster et al., 2006; Moosmüller and Chakrabarty, 2011). Indeed, even though the absorption wavelength dependence is usually represented by a simple power law, it has to be noted that especially when different aerosol components (e.g. Black Carbon, Brown Carbon and mineral dust) contribute to light absorption, the spectral behaviour can be more complicated; this feature is commonly referred to as spectral curvature.

The parameter used to quantify this effect will be hereafter referred to as $d\text{AAE}(\lambda_1, \lambda_2, \lambda_3)$; it represents the spectral curvature of $\sigma_a(\lambda)$, computed as the derivative of AAE as a function of $\ln(\lambda)$. This calculation is similar to the one performed to obtain the curvature of Aerosol Optical Depth (AOD) often used by the AERONET network as a proxy for particle size (Kaufman, 1993; Eck et al., 1999; Schuster et al., 2006). Therefore, $d\text{AAE}(\lambda_1, \lambda_2, \lambda_3)$ was calculated as:

$$d\text{AAE}(\lambda_1, \lambda_2, \lambda_3) = 2 \cdot \frac{\text{AAE}(\lambda_1, \lambda_2) - \text{AAE}(\lambda_2, \lambda_3)}{\ln(\lambda_3/\lambda_1)}$$

where $\lambda_1 < \lambda_2 < \lambda_3$.

It is noteworthy that several $d\text{AAE}$ were calculated using different λ combinations. Finally, $d\text{AAE}(450, 635, 880)$ was selected as it responded well to absorption spectral variations. The 450-880 nm range was preferred to 370-950 nm interval in order to limit the possible bias reported by Zotter et al. (2017) at the shortest wavelength of 370 nm and because $\lambda=880$ nm is the reference λ used by the Aethalometer to retrieve eBC concentration. In addition, AAE calculated using also 370 nm did not show a response to specific aerosol types as significant as the one obtained when using 450 nm.

Aerosol absorption coefficients corrected for multiple scattering and adjusted for different wavelengths were also used to calculate the Single Scattering Albedo (SSA), representing the fraction of light extinction that is scattered. In the present work, SSA was retrieved at 450, 525, and 635 nm as $\text{SSA}(\lambda) = \sigma_s(\lambda) / \sigma_e(\lambda)$.

As pointed out by some authors (e.g. Moosmüller and Chakrabarty, 2011; Costabile et al., 2013; Ealo et al., 2016; Titos et al., 2017) also the SSA wavelength dependence might be useful to give hints of

473

474

475

476

477

478

479

480

481

482

483

484

485

486

487

488

489

490

491

492

493

494

495

496

497

498

499

500

501

502

503

504

505

506

507

508

509

510

511

512

513

514

515

516

517

518

519

520

521

522

523

524

525

526

527

528

529

530

531

variations in aerosol size and composition, as it responds to both physical and chemical properties. Specifically, $dSSA/d\lambda$ can serve as an indicator of the aerosol type especially at sites where Saharan dust transport events are detected (Collaud Coen et al., 2004; Yang et al., 2009; Costabile et al., 2013; Romano et al., 2019). For instance, Valenzuela et al. (2015) exploited spectral SSA to distinguish between so-called dust or non-dust periods, i.e. periods influenced or not by advections of aerosol from the Sahara desert.

Single Scattering Albedo Ångström Exponent (SSAAE) was also computed following Moosmüller and Chakrabarty (2011):

$$SSAAE(\lambda_1, \lambda_2) = SAE(\lambda_1, \lambda_2) - EAE(\lambda_1, \lambda_2)$$

Indeed, as $\sigma_s(\lambda) \approx s \cdot \lambda^{-SAE}$ and $\sigma_e(\lambda) \approx e \cdot \lambda^{-EAE}$ (where s and e are constants), it follows:

$$SSA(\lambda) = \frac{\sigma_s(\lambda)}{\sigma_e(\lambda)} \approx \frac{s}{e} \cdot \frac{\lambda^{-SAE}}{\lambda^{-EAE}} = \frac{s}{e} \cdot \lambda^{-(SAE - EAE)} = \frac{s}{e} \cdot \lambda^{-SSAAE}$$

Since extinction is usually dominated by scattering, SSAAE is likely the difference between two quantities (SAE and EAE) with comparable values. For this reason, in most cases SSA is expected to have a weak wavelength dependence and high uncertainties; therefore, it was not taken into account here. Opposite, the single scattering co-albedo $SSCA = 1 - SSA = \sigma_a(\lambda) / \sigma_e(\lambda)$ has a wavelength dependence which can be represented by the Single Scattering Co-Albedo Ångström Exponent (SSCAA) (Moosmüller and Chakrabarty, 2011), here computed as

$$SSCAA(\lambda_1, \lambda_2) = AAE(\lambda_1, \lambda_2) - EAE(\lambda_1, \lambda_2)$$

It is noteworthy that co-albedo wavelength dependence does not depend on the relative contribution of absorption to extinction but only on the difference in their wavelength dependence. Moreover, being EAE comparable with SAE in most cases, SSCAAE is sensitive to both particle size (via EAE) and composition (through AAE), thus it is itself a combination of intensive optical properties describing different aerosol characteristics.

SSAAE shows the same features too but the range of variability of its absolute values is small compared to SSCAAE for typical atmospheric conditions (i.e. $SSA > 0.5$); thus, in this work SSCAAE was preferred as more effective in discriminating aerosol with different characteristics detected during specific episodes (see Section 4.1).

For all optical parameters calculated with two wavelengths, the widest Nephelometer λ range (450-635 nm) was used to avoid extrapolation of $\sigma_s(\lambda)$ from 635 nm to 880 nm. Indeed, calculations

performed with other couples of wavelengths (450-525 and 525-635) did not show significantly different features; the upper limit at 880 nm was considered for dAAE calculation only.

For the sake of clarity, Table 1 reports a synthesis of the optical parameters used in this work and their definitions.

Parameter name	Definition	Symbol
Single Scattering Albedo	$\sigma_s(\lambda)/\sigma_e(\lambda)$	SSA(λ)
Single Scattering co-albedo	$\sigma_a(\lambda)/\sigma_e(\lambda)=1-SSA(\lambda)$	SSCA(λ)
Scattering Ångström Exponent	$-\ln[\sigma_s(\lambda_1)/\sigma_s(\lambda_2)]/\ln(\lambda_1/\lambda_2)$	SAE(λ_1, λ_2)
Absorption Ångström Exponent	$-\ln[\sigma_a(\lambda_1)/\sigma_a(\lambda_2)]/\ln(\lambda_1/\lambda_2)$	AAE(λ_1, λ_2)
Extinction Ångström Exponent	$-\ln[\sigma_e(\lambda_1)/\sigma_e(\lambda_2)]/\ln(\lambda_1/\lambda_2)$	EAE(λ_1, λ_2)
Absorption spectral curvature	$2[AAE(\lambda_1, \lambda_2)-AAE(\lambda_2, \lambda_3)]/\ln(\lambda_3/\lambda_1)$	dAAE($\lambda_1, \lambda_2, \lambda_3$)
Single Scattering co-albedo Ångström Exponent	$AAE(\lambda_1, \lambda_2)-EAE(\lambda_1, \lambda_2)$	SSCAAE(λ_1, λ_2)

Table 1 Intensive optical parameters used in this work.

3.3 Optical source apportionment

To further confirm the identification of aerosol types (see Section 4.1.2), the well-known Aethalometer model (for detail see e.g. Sandradewi et al., 2008) was applied to estimate the fossil fuel (FF) and biomass burning (BB) contributions to the measured absorption coefficient. Indeed, the availability of multi-wavelength absorption coefficients by the AE33 allowed the apportionment of such contributions using $AAE(FF)=0.9$ and $AAE(BB)=1.68$, as suggested by Zotter et al. (2017) when site-specific values are lacking.

4 Results and Discussion

In the following, a detailed analysis of temporal patterns for intensive optical properties taken into account for aerosol classification is reported.

591
592
593
594
595
596
597
598
599
600
601
602
603
604
605
606
607
608
609
610
611
612
613
614
615
616
617
618
619
620
621
622
623
624
625
626
627
628
629
630
631
632
633
634
635
636
637
638
639
640
641
642
643
644
645
646
647
648
649

4.1 Temporal patterns of aerosol intensive optical properties - episodes and aerosol types identification

Temporal patterns of 1-h averaged SSCAAE(450,635), SAE(450,635), AAE(450,635), dAAE(450,525,635), and dAAE(450,635,880) are shown in Figure 1. High time-resolution temporal behaviour for multi-wavelength scattering, absorption coefficients, and SSA, together with concentration of chemical components and particle number in different size ranges can be found in the Supplementary Material.

As discussed in Section 3, SSCAAE is sensitive to both particle size and composition, thus very high or low values are likely indicative of aerosol with particular properties. During the CARE experiment, SSCAAE had a median value of 0.2 and the 5th and 95th quantiles equal to -0.1 and 1.2, respectively. Interestingly, in some periods SSCAAE values appeared significantly higher than the median value for the campaign; three events with SSCAAE(450,635) values larger than 1 occurred on 3-6 February (hereafter referred to as first episode), 24-25 February (hereafter referred to as second episode), and for a few hours in the afternoon of February 26th (hereafter referred to as third episode).

Temporal patterns of SAE, AAE, and dAAE calculated with two λ triads (exploring different wavelength ranges) were analysed to look for different responses of these intensive properties among the three events during which SSCAAE was almost the same.

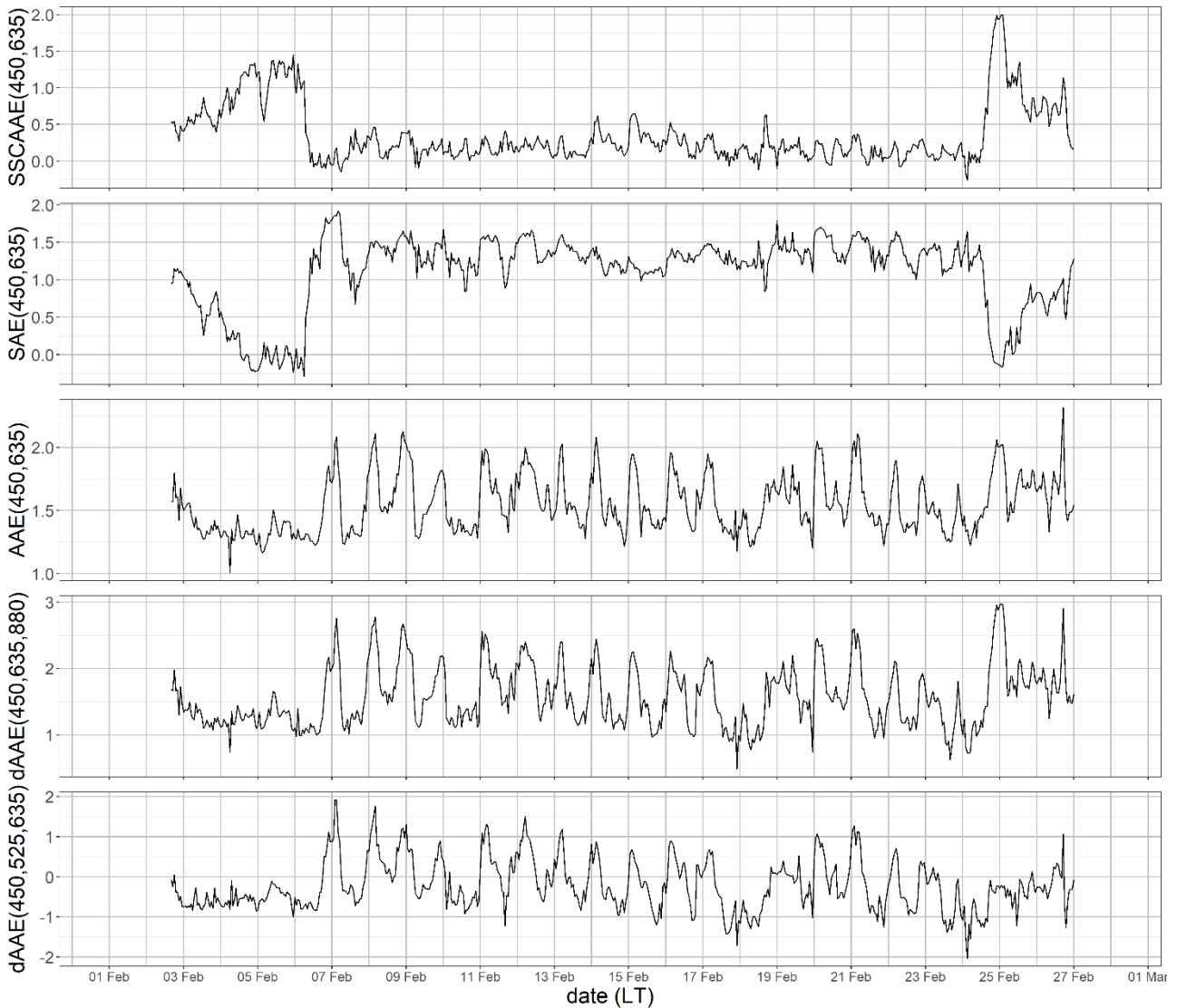


Figure 1 Temporal patterns of SSCAAE(450,635), SAE(450,635), AAE(450,635), dAAE(450,635,880), and dAAE(450,525,635) during the CARE campaign.

Comparing several intensive optical properties (Figure 1), it was evident that the three episodes identified via SSCAAE temporal pattern represented events with different characteristics. In particular, SAE had significant lower values during the first two events and AAE was low in the period 3-6 February, higher during the second episode, and reached its absolute maximum in correspondence to the last one. The absorption spectral curvature dAAE(450,635,880) resembled the AAE(450,635) pattern, whereas dAAE(450,525,635) was not sensitive to the event occurring between February 24th and 25th.

In the next sections, episodes detected looking at intensive optical parameters will be analysed in detail in order to distinguish the aerosol origin and physical-chemical characteristics responsible for

709
710
711
712
713
714
715
716
717
718
719
720
721
722
723
724
725
726
727
728
729
730
731
732
733
734
735
736
737
738
739
740
741
742
743
744
745
746
747
748
749
750
751
752
753
754
755
756
757
758
759
760
761
762
763
764
765
766
767

the observed features in optical properties. In particular, periods characterised by advection-dominated and local sources-dominated aerosols will be addressed with the aim of checking the effectiveness of SSCAAE as the key parameter to quickly identify the presence of specific aerosol events.

4.1.1 Advection-dominated aerosol types

As already mentioned, the first episode was characterised by high SSCAAE values especially between February 3rd and 6th. As shown in Figure 1, SAE(450,635) was low (below 0.5), indicating the predominance of large particles. Moreover, SSA(λ) was quite high (above 0.8) and exhibited a negative wavelength dependence (Figure S4) thus further suggesting a significant contribution of particles with large diameters, as also reported by Takemura et al. (2002) for desert dust and sea salt (with a weaker wavelength dependence). During this period $\sigma_a(\lambda)$ was low (see Figure S3) and AAE(450,635) was small (about 1.3), thus suggesting that the absorption spectral behaviour was dominated by Black Carbon (BC) contribution from local fresh traffic emissions, typically associated to AAE=1, as also shown by Costabile et al (2019). Finally, both dAAE(450,525,635) and dAAE(450,635,880) were lower than the campaign average, confirming a weak wavelength dependence of the absorption coefficient.

All these data together were suggestive of a sea salt advection episode; indeed, sea salt aerosol is generally characterised by quite large particles (from 0.5 to tens of micrometres - Ramachandran, 2018) and it does not typically contribute to $\sigma_a(\lambda)$ wavelength dependence due its negligible absorption coefficient. The attribution to a desert dust event (that can show similar SAE values) was excluded as higher AAE values are typically observed for this aerosol type (as explained in the following).

The sea salt transport episode identified through optical parameters was confirmed by particle number in different size ranges and chemical composition data.

Total particle number in the ranges $1 \mu\text{m} < d_a < 2.5 \mu\text{m}$ and $2.5 \mu\text{m} < d_a < 10 \mu\text{m}$ - that will be referred to as intermodal and coarse fractions, respectively - was calculated. From February 3rd to February 6th a large increase in number concentration of the intermodal and coarse fractions was observed in agreement with the indication given by SSA wavelength dependence and consistently with results shown by Costabile et al. (2019).

768

769

770

771

772

773

774

775

776

777

778

779

780

781

782

783

784

785

786

787

788

789

790

791

792

793

794

795

796

797

798

799

800

801

802

803

804

805

806

807

808

809

810

811

812

813

814

815

816

817

818

819

820

821

822

823

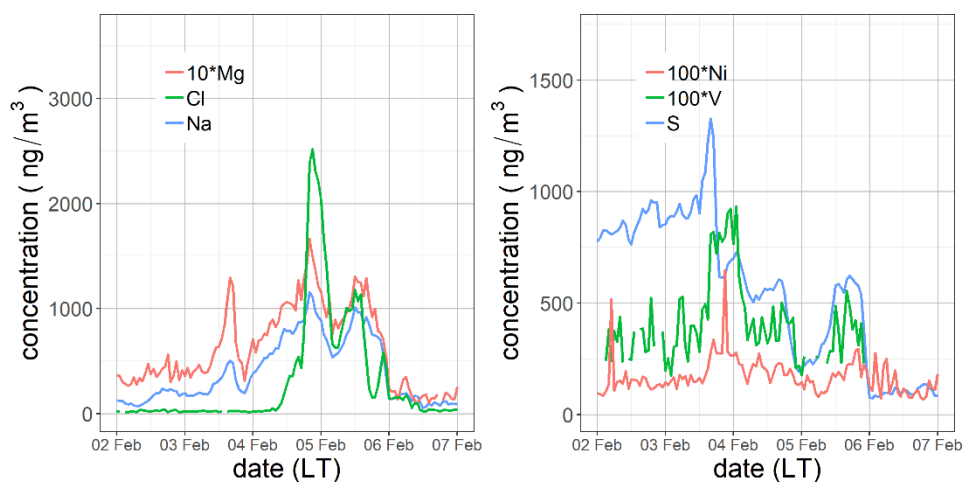
824

825

826

352 During the sea salt episode, particle number concentrations in the intermodal and coarse size
353 fractions were higher and sub-micrometric/intermodal ratio was lower (both of one order of
354 magnitude) than in the rest of the campaign. It is noteworthy that during the period 3-6 February
355 three sub-events were identified due to significant differences in aerosol properties. Indeed, the
356 ratio of intermodal/coarse fractions was similar to previous days until the late afternoon of February
357 3rd (even though concentration of super-micrometric aerosol is already high), it subsequently
358 peaked in the evening of February 4th and increased again in late morning in February 5th. It is
359 noteworthy that these sub-events can also be detected by a more detailed analysis of SSCAE,
360 exhibiting a first small peak contemporary to the period of stable intermodal/coarse on February
361 3rd, and two periods with values higher than 1 interrupted by a minimum corresponding to low SSA
362 values and an increasing number concentration of sub-micrometric particles compared to the one
363 in intermodal and coarse size fractions (Figure S8).

364 A focus on chemical composition can be seen in Figure 2, that represents temporal patterns of Na,
365 Mg, Cl, V, Ni and S concentrations measured by PIXE analysis on PM2.5 streaker samples.



367

368

369

370

371

372

373

374

375

376

377

378

379

380

381

382

383

384

385

386

Figure 2 Concentrations of Na, Mg, Cl, V, Ni, and S in PM2.5 during the CARE campaign.

370 The sea salt advection episode (see Figure 2) was characterised by a simultaneous increase in Na,
371 Cl, and Mg concentrations - reaching 1158, 2518, and 362 ng/m³, respectively - compared to average
372 values of 92, 38, and 33 ng/m³ detected during the rest of the campaign. Sea salt aerosol fresh
373 emissions are typically identified through diagnostic ratios for bulk sea water (Seinfeld and Pandis,
374 1998), e.g. Cl/Na (1.8) and Mg/Na (0.12). It has to be noted that sea salt Cl in aerosol particles can
375 be depleted due to heterogeneous reactions with other compounds occurring in the atmosphere

827
828
829 376 (Seinfeld and Pandis, 1998), whereas Mg and Na are not involved in these processes; as a
830 377 consequence, the Cl-to-Na ratio measured in sea salt aerosol can be lower than the one calculated
831 378 based on bulk sea water composition, while Mg-to-Na ratio is maintained. As Na and Mg can be
832 379 originated by multiple sources (e.g. sea salt, crustal material, industrial processes), when using the
833 380 above mentioned diagnostic ratio only the contribution to the concentration of these elements due
834 381 to sea salt should be taken into account. In this work, the elemental concentration was assessed by
835 382 PIXE, therefore the concentration of sea salt Na (ssNa) was calculated following Diapouli et al.
836 383 (2017). During the first episode, the ssNa-to-Na ratio was on average 0.95 ± 0.04 , therefore the total
837 384 Na concentration was used to calculate diagnostic ratios, to avoid further uncertainties related to
838 385 assumptions in the ssNa calculation. In the first sub-event (February 3rd) Mg-to-Na ratio (0.16 ± 0.08)
839 386 was fairly in agreement with the expected value of 0.12 while Cl-to-Na ratio was much lower
840 387 (0.06 ± 0.02) than the one expected for fresh sea salt. The diagnostic ratios were thus suggesting that
841 388 aged sea salt particles impacted on the sampling site and that Cl was likely depleted by atmospheric
842 389 reprocessing during the plume transport (Seinfeld and Pandis, 1998). Indeed, on February 3rd
843 390 (afternoon) peaks in V, Ni, and S concentrations - well known tracers for ship emissions (Viana et al.
844 391 2009) - were also registered. These chemical fingerprints confirmed that this first sub-event
845 392 corresponded to the impact of a plume of aged and polluted marine aerosol.
846 393 An increase in SSCAAE and peaks in Cl, Na, and Mg concentrations characterised the second sub-
847 394 event (February 4th). The Cl/Na and Mg/Na ratios were 1.79 ± 0.75 and 0.14 ± 0.01 , respectively, i.e.
848 395 comparable to diagnostic ratios for fresh sea salt. In this episode no significant contribution from
849 396 anthropogenic components (e.g. V, Ni, EC) was observed, thus indicating the advection of clean
850 397 marine air mass to the sampling site.
851 398 On February 5th, a third SSCAAE peak was registered and the aerosol characteristics were similar to
852 399 the previous period but for smaller Cl/Na ratio (0.88 ± 0.38) and concentrations of S, V, and Ni, thus
853 400 indicating the aging of the sea salt aerosol reaching the CARE site.
854 401 In between the second and third peak, a decrease in SSCAAE (Figure 1), SSA (Figure S4), and
855 402 concentrations of typical sea salt components together with increases in EC and $\sigma_a(\lambda)$ accounted for
856 403 a temporary predominance of local urban emissions, as further confirmed by a corresponding
857 404 decrease in wind speed (not shown).
858 405 The assignment of the observed properties to the advection of marine aerosol was also supported
859 406 by back trajectory analysis (see Figure S9).

886
887
888
889
890
891
892
893
894
895
896
897
898
899
900
901
902
903
904
905
906
907
908
909
910
911
912
913
914
915
916
917
918
919
920
921
922
923
924
925
926
927
928
929
930
931
932
933
934
935
936
937
938
939
940
941
942
943
944

407 The SSCAAE peak (Figure 1) registered between February 24th and 25th highlighted the second
408 episode, when low SAE(450,635) (below 0.5) and high AAE(450,635) (above 1.5) were also observed.
409 In addition, a different response by dAAE(450,635,880) and dAAE(450,525,635) was recorded with
410 high and low values, respectively, thus pointing at the smaller absorption spectral curvature at
411 longer wavelengths compared to the shorter ones. In the literature, SAE with values comparable to
412 zero have often been reported as an indication of desert dust detected at the studied site (e.g.
413 Andreae et al., 2002; Yang et al., 2009; Costabile et al., 2013; Ealo et al., 2016; Titos et al., 2017;
414 Lihavainen et al., 2017; Horvath et al., 2018; Romano et al; 2019). Indeed, SAE is linked to particle
415 size (as described in Section 3) and desert aerosol is generally characterised by a large-sized particle
416 contribution greater than in typical urban background PM. Advection events of desert aerosol have
417 usually been associated to AAE significantly larger than one (in the range 1.2-3.5 – Collaud Coen et
418 al., 2004; Fialho et al., 2006; Yang et al., 2009; Lee et al., 2012; Costabile et al., 2013; Lihavainen et
419 al., 2017; Romano et al., 2019), in contrast to sea salt aerosol (exhibiting similar SAE but lower AAE).
420 Moreover, it has been shown (e.g. Collaud Coen et al., 2004; Yang et al., 2009) that a non-negligible
421 SSA wavelength dependence and more specifically negative SSAAE values, can be attributed to the
422 predominance of large particles, usually associated with desert dust.
423 All these considerations, together with the combined temporal patterns of different optical
424 properties (see Figures 1, S2, S3, S4) were suggestive of an episode of desert dust transported to
425 the CARE sampling site between February 24th and 25th. To confirm the hypothesis of a Saharan dust
426 transport, size-segregated particle number and chemical composition were also investigated. The
427 sub-micrometric/intermodal ratio showed a sharp decrease compared to days close in time and
428 concentration of dust elemental tracers showed a huge increase (Figure 3) (Nava et al., 2012; Gobbi
429 et al., 2019).

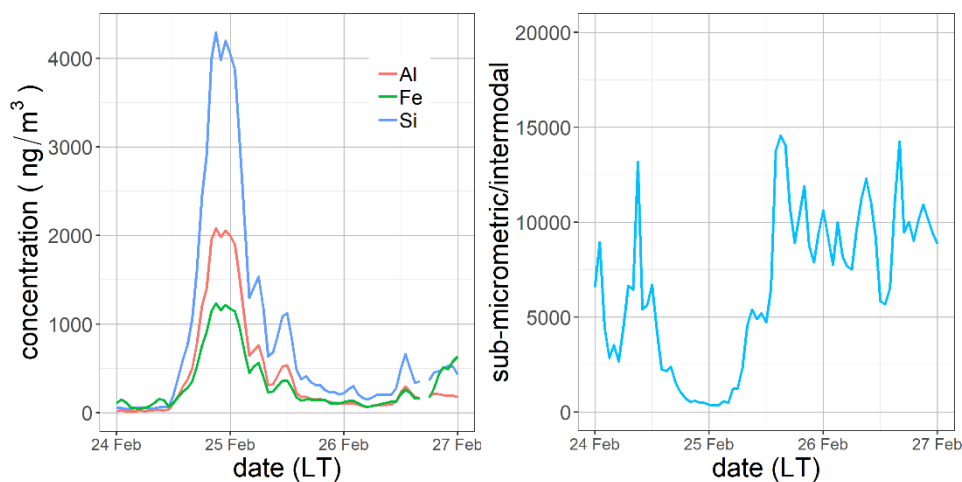


Figure 3 On the left: concentrations of Al, Si, and Fe in PM_{2.5}. On the right: Ratio of sub-micrometric/intermodal particle number. The period represented refers to the Saharan dust episode.

Back-trajectory analysis evidenced that the air mass reaching the CARE site during the night between February 24th and 25th had passed over the Sahara desert at ground level on February 22nd and then reached the sampling site after crossing the Mediterranean at higher altitudes (see Figure S10).

4.1.2 Local sources dominated aerosol types

Another feature shown by SSCAAE was a narrow peak on February 26th afternoon (Figure 1), when smoke was seen by researchers working at the CARE site. Indeed, around 13:00 (LT) a large amount of smoke was noticed at Stadium Caracalla and at 18:00 (LT) smoke was smelled at Terme di Caracalla, nearby the CARE sampling site.

As shown in Figure 1, during this episode AAE(450,635) reached its highest value indicating the presence of relatively small particles (SAE was about 1) with an absorption wavelength dependence stronger than the one of BC. This was likely due to the presence of Brown Carbon (BrC) and it was consistent with the presence of combustion-generated emissions. As reported in Figure 4, a sharp increase in the biomass burning tracer BBOA was observed during the event (Figure 4); it is noteworthy that the concomitant occurrence of AAE(450,635) and dAEE(450,635,880) peaks reinforced the attribution to a short fire episode characterised by absorbing particles with a stronger absorption at shortest wavelengths. The Radon temporal pattern (Figure S11) revealed that the fire episode occurred during well-mixed atmospheric condition (low Radon values) while soon after a strong atmospheric stability affected the monitoring site thus promoting the pollutants accumulation (high Radon values and BBOA peak).

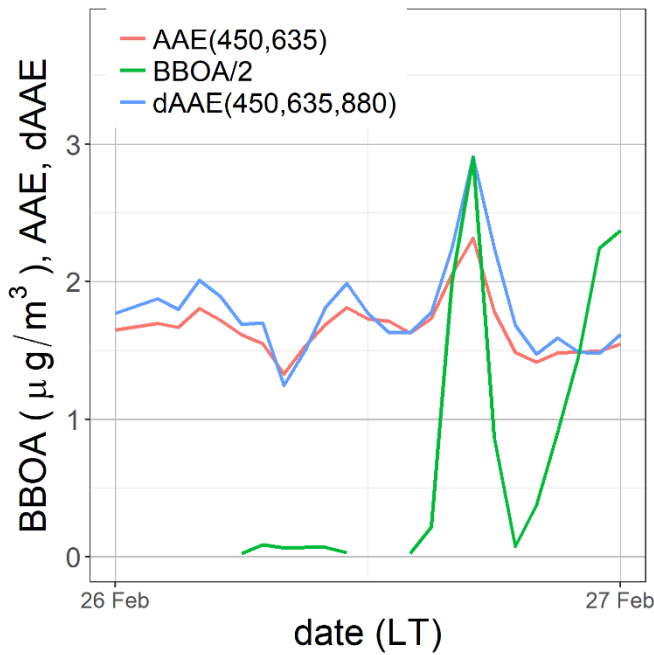


Figure 4 Temporal patterns of AAE(450,635), dAAE(450,635,880), and BBOA concentration during the biomass burning event of February 26th, 2017.

The central part of the CARE campaign (from February 11th to 22nd) was characterised by atmospheric stability (see Figure S11), with low wind speeds and clear sky. During this period, high $\sigma_a(635)$ values ($>50 \text{ Mm}^{-1}$) especially in the evening were recorded. Low SSA(635) values (very often below 0.8), SSCAAE(450,635) <0.65 and mean SAE(450,635) and AAE(450,635) values of 1.33 ± 0.19 and 1.57 ± 0.23 , respectively, were observed. These aerosol characteristics pointed at a mixture of local emissions from traffic rush hours and biomass burning used for domestic heating. Indeed, the SAE and AAE values indicated a dominance of small particles with quite a strong absorption wavelength dependence, as the one caused by BrC. In the central period of the campaign wind speed was low (average \pm standard deviation: $1.46\pm0.89 \text{ m/s}$) suggesting a major role of local aerosol sources.

Multi-wavelength high-time resolved absorption coefficient data were used to perform an optical source apportionment through the well-known Aethalometer model (see Section 3). The two sources considered in the model (fossil fuels - FF and biomass burning - BB) should give the highest contributions at 880 nm and 450 nm (i.e. the longest and the shortest wavelengths used here for aerosol absorption properties) due to the different absorption spectral dependence of aerosol particles emitted by FF and BB. Therefore, $\sigma_a(880)(\text{FF})$ and $\sigma_a(450)(\text{BB})$ were taken as representative

parameters for periods dominated by traffic and biomass burning emissions, respectively, as also confirmed by the similarity in temporal patterns of HOA and BBOA (Figure 5).

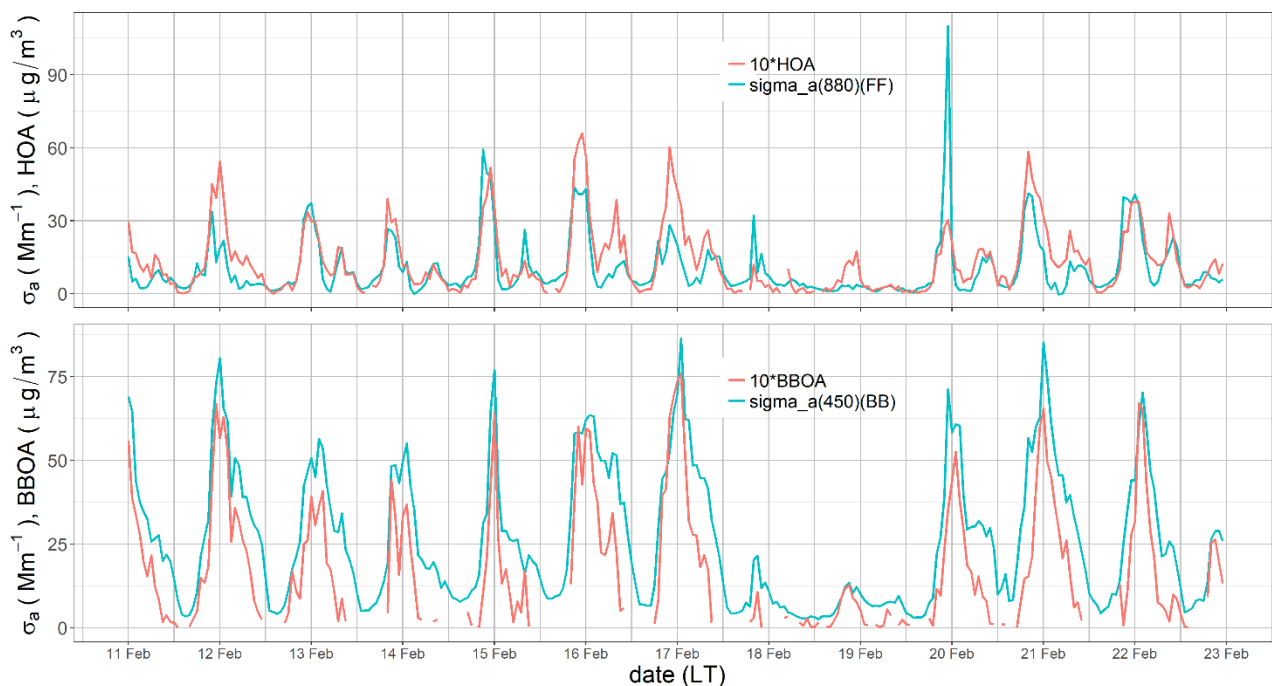


Figure 5. Top panel: Temporal patterns of $\sigma_a(880)(FF)$ and HOA concentration. Bottom panel Temporal patterns of $\sigma_a(450)(BB)$ and BBOA concentration. Absorption coefficients were averaged over 1 hour to match OAs time resolution. Only data in the central part of the campaign (February 11-22) are represented.

Increased concentration of EC and HOA, typically associated to traffic emissions, were detected as well (Figures S6 and S7).

In Figure 6 diurnal cycles of number concentration for ultrafine particles (less than $0.1 \mu\text{m}$ in size, UFPs) and for particles in the size range $0.1\text{-}1 \mu\text{m}$ during working days are shown; as expected, UFPs peaked during traffic rush hours, confirming that the dominant contribution during these hours was given by very small particles from fresh vehicular emissions. In addition, particles in the $0.1\text{-}1 \mu\text{m}$ size fraction showed similar peaks but remained higher during the night, probably due to the effect of emissions from domestic heating combined with the daily evolution of the boundary layer height.

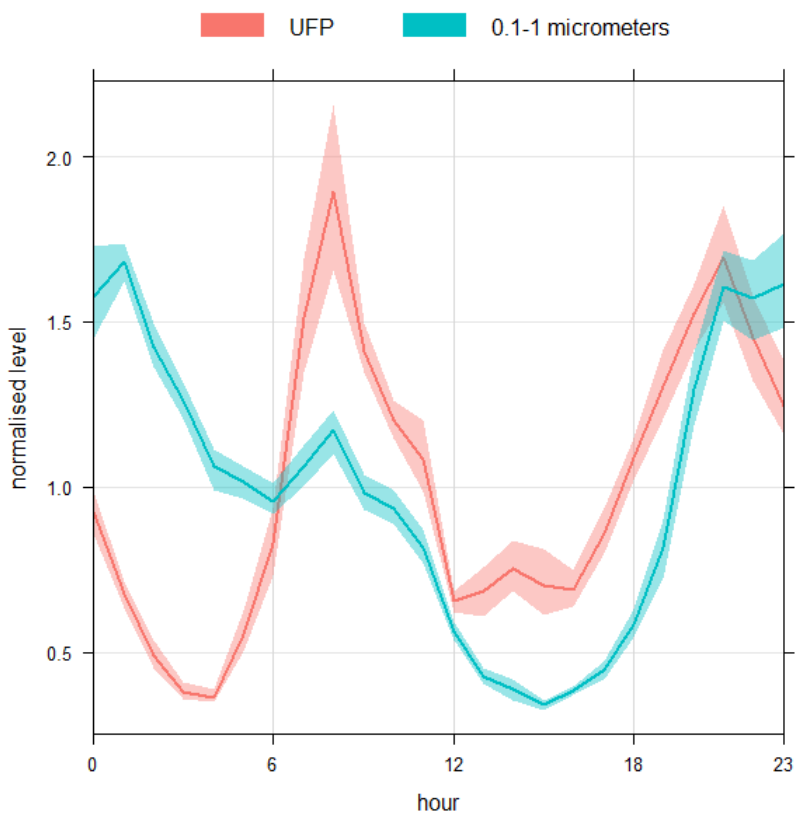


Figure 6 Diurnal variation (normalised, in local time) of particle number concentration for UFPs and particles in the 0.1-1 μm size fraction. Data refer to the central part of the campaign (February 11-22).

4.2 Graphical aerosol classification schemes

Some aerosol classification schemes based on the combination of aerosol properties will be presented in the following with the aim of providing graphical tools that can be useful to quickly distinguish specific events out of a complex dataset comprising optical variables.

Ranges of intensive optical properties allowing to best discriminate among aerosol types identified during the CARE campaign were derived based on the comprehensive analyses previously reported.

In

Table 2 ranges of the optical parameters used to classify each type are listed; all the reported conditions should be met in order to robustly identify different aerosol types.

In this work, six main aerosol types were classified. The identification of aerosol particles originated by vehicular traffic and biomass burning during the atmospheric stable period (see Section 4.1.2) was the most difficult task as the intensive optical properties were not sufficient to discriminate the two aerosol types. Therefore, the information retrieved by the Aethalometer model (see Sections 3

and 4.1.2) was added to identify periods when aerosol was dominated by traffic or biomass burning emissions.

Aerosol Type	SSCAAE (450,635)	SAE (450,635)	AAE (450,635)	dAAE (450,635,880)	dAAE (450,525,635)	SSA (635)	σ_a (450)(BB)	σ_a (880)(FF)
Dust	>0.6	<0.4	>1.5	>1.6	<0.2	>0.8	-	-
Sea	>0.6	<0.4	<1.5	<1.7	<0.2	>0.8	-	-
Polluted marine	0.6-0.9	0.3-0.8	<1.5	1.0-1.5	-1.0-0.0	>0.9	-	-
Fire	>0.8	>0.7	>1.8	>2.0	>0	-	-	-
Traffic	<0.2	-	-	-	-	<0.85	-	>8
BB	<0.65	-	-	-	-	-	>20	-

Table 2 Ranges of optical parameters useful to classify aerosol types. σ_a is given in Mm^{-1} . Note that “dust” stands for desert aerosol; “sea” and “polluted marine” stand respectively for the first sub-event and the second and third sub-events of the sea salt aerosol advection episode; “fire” stands for the short biomass burning episode; “traffic” indicates periods dominated by traffic emissions; “BB” indicates periods dominated by the contribution of biomass burning for residential heating.

Together, the polluted and the clean marine air masses advected to the sampling site occurred in 7.9% of the cases (i.e. whole CARE dataset); desert dust data covered 2.7% of the cases; data referring to the fire event were 0.3% of the cases; traffic and biomass burning data represented 20.6% and 17.2% of the cases, respectively.

Table 3 reports ranges of AAE, SAE, and SSA that were used in previous studies to classify aerosol types. Indeed, AAE and SAE were the most commonly employed parameters, usually combined to assess aerosol origin. In some works, information about SSA was added to help the distinction.

Reference	Columnar/ in situ properties	Wavelengths (nm)	Aerosol type	AAE	SAE	SSA
Bahadur et al., 2012	Columnar (AERONET)	440, 675	Dust	>1.5	<0.5	-
			Biomass burning	0.5-2	1-2	-
			Urban fossil	<1.5	0.5-2	-

Cazorla et al., 2013	Columnar (AERONET)	440, 675	Dust	>1.5	<1	
			Coated large particles	<1	<1.5	-
			OC dominated	>1.5	>1.5	-
			EC dominated	<1	>1.5	-
Cappa et al., 2016	In-situ	532, 600 (AAE) 450, 550 (SAE)	Dust	>2	<0.2	-
			Large particle/low absorption mix	<1	<1	-
			Strong BrC	>2	>1.5	-
			BC dominated	1.0-1.5	>1	-
Costabile et al., 2013	In-situ	467, 660 (SSA at 530 nm)	Dust	2	<0.5	>0.85
			Marine	>2	<0.5	> 0.95
			BC dominated	<1.5	>2	<0.8
			Brown carbon	>2.5	0.5-2	>0.9
Schmeisser et al., 2017	In-situ	450, 700	Biomass burning	<2	1-3	<0.85
			Dust	>1.5	<1	-
			Polluted marine	0.9-1.4	0.7-1.7	-
			Remote marine	0.5-1.5	<1	-
Romano et al., 2019	In-situ	470, 660	Continental polluted	1-1.5	>1.4	-
			Dust	>2	<-0.2	-
			Marine	<1.2	<0	-
Rupakheti et al., 2019	Columnar (AERONET)	440-870 (EAE instead of SAE, SSA at 675 nm)	Dust	1.0-3.0	0.0-0.4	0.88-0.96
			Biomass burning	1.1-2.3	0.8-1.7	0.82-0.91
			Urban/Industrial	0.6-1.3	0.8-1.6	0.89-0.96
This study	In-situ	450, 635 (SSA at 635 nm)	Dust	>1.5	<0.4	>0.8
			Sea	<1.5	<0.4	>0.8
			Polluted marine	<1.5	0.3-0.8	>0.9
			Fire	>1.8	>0.7	-
			Traffic	<1.7	>0.7	<0.85
			BB	>1.5	>1.0	-

Table 3 AAE, SAE and SSA values used to classify aerosol types in literature works and this study.

Table 3 shows that AAE and SAE values used in this study are generally in agreement with literature values; differences may be due to the wavelengths used in the calculation of intensive optical properties, as well as to the fact that columnar or in-situ properties are employed. It has to be noted that episode-discriminating values reported in Table 2 are in principle wavelength-dependent, thus they are expected to be different if other wavelengths are employed for the calculation of intensive

optical properties. Moreover, they may differ depending on the location and season, due to the mixing of pure aerosol types with local emissions, that could affect optical properties. Therefore, in the perspective of using such approach in monitoring networks, it is strongly suggested to perform a preliminary study to check the most suitable ranges of optical variables. Nevertheless, graphical frameworks presented in the following can serve as guides to identify possible episodes simply observing where data are located in each plot.

After identification and selection of the events, data with 5-min resolution were represented in some graphical schemes. In Figures 7 and 8, the left panel represents data classified as a particular aerosol type according to the methodology described above, whereas the right panel shows the rest of the data (not classified). Data points belonging to different aerosol types are distinguished using different symbols.

4.2.1 AAE vs SAE plot

AAE vs. SAE plot was originally developed in literature for data retrieved from the AERONET network (Russell et al., 2010) and then refined by Cazorla et al. (2013). Other authors (e.g. Cappa et al., 2016; Romano et al., 2019) applied the same methodology to in-situ ground-based data. The graphical classification scheme in Figure 7 is the AAE vs SAE plot, colour-coded by SSA(635) following Costabile et al. (2013).

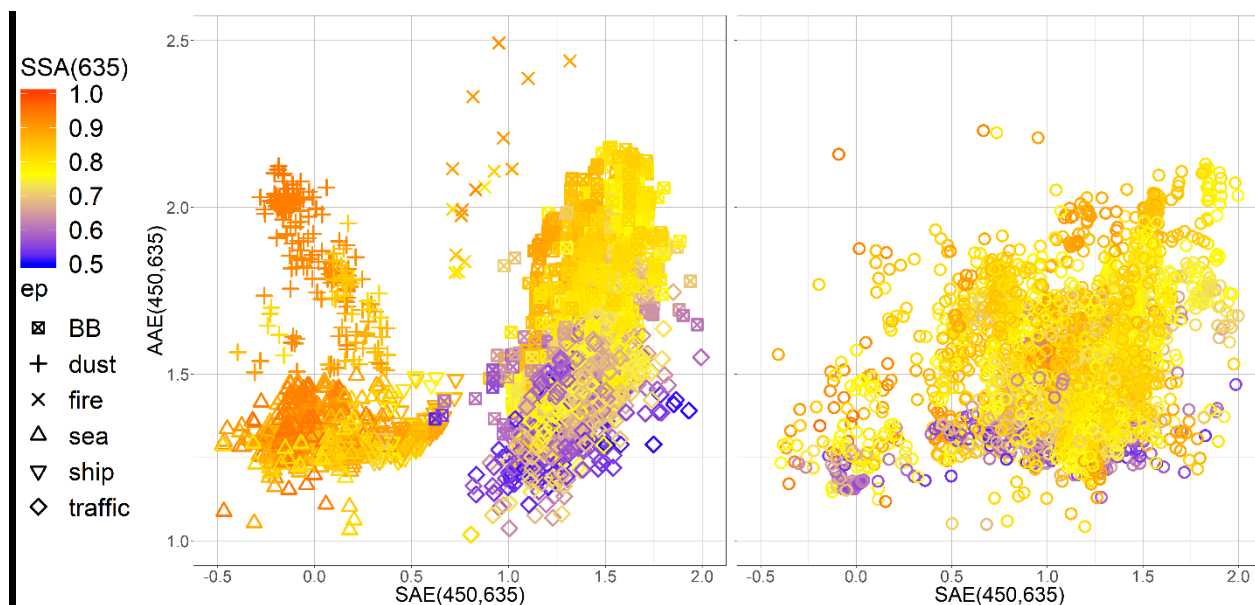


Figure 7 AAE vs SAE plot colour-coded by SSA(635). On the left: data related to an aerosol type. On the right: all the remaining – i.e. non classified – data. Different symbols represent data of identified

1358
1359
1360 aerosol types. BB stands for biomass burning. Note that “ship” stands for the polluted marine event
1361 and “fire” for the short biomass burning event.
1362
1363

1364
1365 As expected from the values reported in the look-up table (Table 2), when representing episodes in
1366 a plane, the corresponding data points are placed in different areas. It can be noted that “ship”,
1367 “sea”, “dust” and “fire” data are largely not mixed with non-classified data in the respective plot
1368 areas, as emerges also from Figure 7 (right panel), where some zones of the graph are not covered
1369 by points. Points classified as “ship” or “sea” (i.e. marine air masses) are the majority of data in the
1370 area defined by ($SAE < 0.8$ and $AAE < 1.5$); they were considered together since they are mixed in the
1371 graphical scheme. “Traffic” and “BB” points, although not completely overlapped, are also mixed
1372 with each other, reflecting the mixture of local sources contributing to atmospheric aerosol during
1373 the central part of the experiment.
1374
1375

1376
1377 The AAE vs SAE plot together with the third coordinate (SSA) helped in the visual discrimination of
1378 episodes, even though no ideal SAE, AAE, and SSA ranges were found to correctly classify the first
1379 sea salt advection (dominated by ship emissions) without the combined use of SSCAAE and dAAE,
1380 that allowed to distinguish this aerosol sub-type.
1381
1382

1383
1384 Therefore, a detailed analysis of temporal patterns of different intensive optical properties
1385 (especially SSCAAE) gives a more complete set of information which can be used to distinguish all
1386 the events that may have occurred during a campaign. Moreover, for more complex mixtures of
1387 aerosol from different sources (when atmospheric stability occurs), the additional information from
1388 high-time resolved extensive optical properties is necessary to separate the dominant contribution.
1389
1390

1391 1392 1393 1394 1395 1396 **4.2.2 SSCAAE vs dAAE plot**

1397
1398 The second graphical framework proposed is a SSCAAE vs dAAE plot (Figure 8), colour-coded by
1399 SSA(635). As far as the authors know, no other study has used a similar scheme to distinguish
1400 episodes and aerosol types.
1401
1402
1403
1404
1405
1406
1407
1408
1409
1410
1411
1412
1413
1414
1415
1416

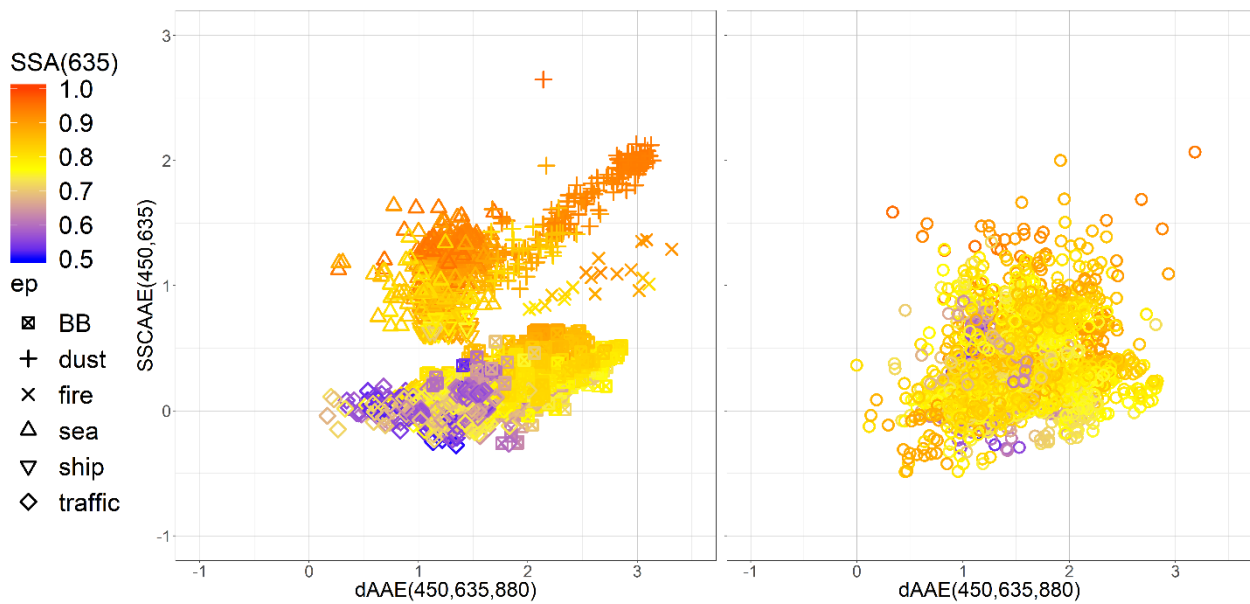


Figure 8 SSCAAE vs dAAE plot colour-coded by SSA(635). On the left: data related to an aerosol type. On the right: all the remaining - i.e. non classified - data. Different symbols represent data of identified aerosol types. BB stands for biomass burning. Note that “ship” stands for the polluted marine event and “fire” for the short biomass burning event.

This new scheme (Figure 8) confirmed the potential of SSCAAE as a key parameter for episodes identification. Indeed, except for urban aerosol, all the other aerosol types were characterised by $SSCAA E(450,635) > 0.5$. The combination with $dAAE(450,635,880)$ helped to discriminate events, since this parameter responds to non-uniform absorption spectral dependence that can be different for episodes with similar SSCAAE values. For instance, this was the case of “sea” and “fire” aerosol types, characterised respectively by mean $SSCAA E(450,635)$ equal to 1.16 ± 0.18 and 1.05 ± 0.17 and mean $dAAE(450,635,880)$ of 1.25 ± 0.21 and 2.65 ± 0.39 , respectively.

Also in this case episodes are placed in different regions of the plane and some areas are not well covered by data points when considering only non-classified data (Figure 8 - right). In this graphical framework some aerosol types (in particular “dust”, and to a less extent “fire”) show an almost linear relationship between SSCAAE and dAAE. Finally, local-sources dominated periods are characterised by an almost λ -independent co-albedo ($SSCAA E \approx 0$) and by an increase in the absorption spectral curvature as the contribution of biomass burning emissions increases compared to the one from vehicular traffic.

The SSCAAE vs dAAE plot and AAE vs SAE plot are useful to provide a first hint about episodes and aerosol typologies. Nevertheless, 2D plots areas do not correspond uniquely to different aerosol types; especially aerosol mixtures impacted by local sources are not distinguishable from not

classified data, since zones where the two populations are located in the plots overlap. This is a limitation of 2D plots when plotting all data (both classified and unclassified) together as urban aerosol mixtures produce a cloud of points comprehending both traffic- and biomass burning-related emissions. In complex situations, it is the separate study of temporal patterns of all the intensive optical parameters (SSCAAE, SAE, AAE, and dAAE) that can provide further information to distinguish aerosol with different origins.

Conclusions

Aerosol physical-chemical and optical properties measured at high time resolution during the CARE experiment were analysed to classify different aerosol types, both from advection episodes and by local source emissions.

In particular, this study was focused on multi-wavelength optical properties measured by widespread on-line instrumentation (i.e. Nephelometer, Aethalometer, and MAAP). It has to be noted that, when analysing such kind of data, attention has to be paid to their interpretation and elaboration, since they require non-negligible corrections to take into account biases due to the filter matrix (e.g. for the Aethalometer) and for truncation effects (for the Nephelometer).

In this work, scattering and absorption coefficients were employed to obtain several intensive optical parameters. At the CARE monitoring site, the wavelength dependence of the co-albedo (SSCAAE) was the most effective parameter in discriminating between aerosol particles dominated by air masses advection or influenced by local emissions; SSCAAE can be, therefore, a good candidate to be tested in similar studies in the future. Nevertheless, even exploiting the high time resolution, only a combination of several optical properties led to a better classification of different aerosol types. Chemical composition and size distribution data were employed to confirm the advection episodes and aerosol types identified by the optical parameters. Due to difficulties in disentangling local source emissions impacting on aerosol properties in atmospheric stagnant conditions, the well-known Aethalometer model was applied which helped in identifying the contribution of traffic and biomass burning to the absorption coefficient measured at different wavelengths.

Graphical classification schemes developed in this work represented useful tools to get a first classification of aerosol particles based on optical intensive parameters for specific aerosol advection events. At the same time, this work clearly showed that a more robust aerosol

1535
1536
1537
1538
1539
1540
1541
1542
1543
1544
1545
1546
1547
1548
1549
1550
1551
1552
1553
1554
1555
1556
1557
1558
1559
1560
1561
1562
1563
1564
1565
1566
1567
1568
1569
1570
1571
1572
1573
1574
1575
1576
1577
1578
1579
1580
1581
1582
1583
1584
1585
1586
1587
1588
1589
1590
1591
1592
1593

classification can be obtained by observing temporal patterns of optical parameters. Although based on the analysis of few episodes, the complete aerosol chemical speciation and the availability of number size distributions confirmed the nature of the episodes detected by optical parameters.

The methodology here applied can be replicated at any site to generate specific look-up tables or using the one reported in this work at sites with similar characteristics; this approach can be useful to discriminate in near-real-time between pollution vs. natural sources-driven high PM events in environmental monitoring networks using optical parameters only. Of course, this procedure is much simpler than e.g. the methodology officially accepted by the European Commission (see e.g. Querol et al., 2019) to estimate the African dust outbreaks but provides hints also on the impact from other aerosol sources.

Author contributions: SV drafted the paper and performed the data analysis; RV proposed the topic of this paper and contributed to the the synthesis of the results; VB, ACF, and GV collaborated to data analysis and interpretation; FB, FC, LDL, and GPG took care of the whole campaign, performed optical data measurements, data reduction and contributed to data interpretation; GC, FL, and SN carried out streaker sampling, PIXE analysis, EC/OC measurements and data analysis; MG and EP provided ACSM data and performed PMF analysis to retrieve BBOA, HOA, and OOA data; AW provided MAAP data. All authors contributed to the interpretation of the results obtained with the approach here described and revised the manuscript content giving a final approval of the version to be submitted. RV and SV reviewed the paper addressing reviewers' comments.

Declaration of interest: The authors declare no conflict of interest.

Data availability: The data in the study are available from the authors upon request (roberta.vecchi@unimi.it).

References

Alas H.D.C., Weinhold K., Costabile F. Di Ianni A., Müller T., Pfeifer S., Di Liberto L., Turner J.R., and Wiedensohler A., 2019. Methodology for High Quality Mobile Measurement with Focus on Black

1594
1595
1596
1597
1598
1599
1600
1601
1602
1603
1604
1605
1606
1607
1608
1609
1610
1611
1612
1613
1614
1615
1616
1617
1618
1619
1620
1621
1622
1623
1624
1625
1626
1627
1628
1629
1630
1631
1632
1633
1634
1635
1636
1637
1638
1639
1640
1641
1642
1643
1644
1645
1646
1647
1648
1649
1650
1651
1652

669 Carbon and Particle Mass Concentrations. *Atmos. Meas. Tech.* 12, 4697-4712;
670 <https://doi.org/10.5194/amt-12-4697-2019>.

671 Andreae T.W., Andreae M.O., Ichoku C., Maenhaut W., Cafmeier J., Kamieli A., Orłowski L., 2002.
672 Light scattering by dust and anthropogenic aerosol at a remote site in the Negev desert, Israel.
673 *Journal of Geophysical Research* 107, D2, 4008, 10.1029/2001JD900252

674 Bahadur R., Praveen P.S., Xu Y., and Ramanathan V., 2012. Solar absorption by elemental and brown
675 carbon determined from spectral observations. *PNAS* 109, 43

676 Barnaba F. and Gobbi G.P., 2004. Aerosol seasonal variability over the Mediterranean region and
677 relative impact of maritime, continental and Saharan dust particles over the basin from MODIS data
678 in the year 2001. *Atmospheric Chemistry and Physics* 4, 2367–2391

679 Barnaba F., Bolignano A., Di Liberto L., Morelli M., Lucarelli F., Nava S., Perrino C., Canepari S., Basart
680 S., Costabile F., Dionisi D., Ciampichetti S., Sozzi R., and Gobbi G.P., 2017. Desert dust contribution
681 to PM10 loads in Italy: Methods and recommendations addressing the relevant European
682 Commission Guidelines in support to the Air Quality Directive 2008/50. *Atmospheric Environment*
683 161, 288-305; <http://dx.doi.org/10.1016/j.atmosenv.2017.04.038>

684 Bond T.C. and Bergstrom R.V., 2006. Light Absorption by Carbonaceous Particles: An Investigative
685 Review. *Aerosol Science and Technology* 40:27–67; DOI: 10.1080/02786820500421521

686 Calzolari G., Lucarelli F., Chiari M., Nava S., Giannoni M., Carraresi L., Prati P., Vecchi R., 2015.
687 Improvements in PIXE analysis of hourly particulate matter samples. *Nucl. Instr. Meth. B*, 363, 99–
688 104; <https://doi.org/10.1016/j.nimb.2015.08.022>

689 Canonaco F., Crippa M., Slowik J.G., Baltensperger U., Prévôt A.S.H., 2013. SoFi, an IGOR-based
690 interface for the efficient use of the generalized multilinear engine (ME-2) for the source
691 apportionment: ME-2 application to aerosol mass spectrometer data. *Atmos. Meas. Tech.* 6, 3649–
692 3661; doi:10.5194/amt-6-3649-2013

693 Cappa C.D., Kolesar K.R., Zhang X., Atkinson D.B., Pekour M.S., Zaveri R.A., Zelenyuk A., and Zhang
694 Q., 2016. Understanding the optical properties of ambient sub- and supermicron particulate matter:
695 results from the CARES 2010 field study in northern California. *Atmospheric Chemistry and Physics*
696 16, 6511–6535; doi:10.5194/acp-16-6511-2016

697 Cazorla A., Bahadur R., Suski K.J., Cahill J.F., Chand D., Schmid B., Ramanathan V., and Prather K.A.,
698 2013. Relating aerosol absorption due to soot, organic carbon, and dust to emission sources

1653
1654
1655
1656 699 determined from in-situ chemical measurements. Atmospheric Chemistry and Physics 13, 9337–
1657 700 9350; doi:10.5194/acp-13-9337-2013
1658
1659 701 Collaud Coen M., Weingartner E., Schaub D., Hueglin C., Corrigan C., Henning S., Schwikowski M.,
1660 702 and Baltensperger U., 2004. Saharan dust events at the Jungfrauoch: detection by wavelength
1661 703 dependence of the single scattering albedo and first climatology analysis. Atmospheric Chemistry
1662 703 and Physics 4, 2465–2480; www.atmos-chem-phys.org/acp/4/2465/
1663 704
1664 704 Collaud Coen M., Weingartner E., Apituley A., Ceburnis D., Fierz-Schmidhauser R., Flentje H.,
1665 705 Henzing J.S., Jennings S.G., Moerman M., Petzold A., Schmid O., and Baltensperger U., 2010.
1666 706 Minimizing light absorption measurement artifacts of the Aethalometer: evaluation of five
1667 707 correction algorithms. Atmos. Meas. Tech., 3, 457–474; www.atmos-meas-tech.net/3/457/2010/
1668 708
1669 708 Costabile F., Barnaba F., Angelini F., and Gobbi G.P., 2013. Identification of key aerosol populations
1670 709 through their size and composition resolved spectral scattering and absorption. Atmospheric
1671 710 Chemistry and Physics 13, 2455–2470; doi:10.5194/acp-13-2455-2013
1672 711
1673 711 Costabile F., Alas H., Aufderheide M., Avino P., Amato F., Argentini S., Barnaba F., Berico M.,
1674 712 Bernardoni V., Biondi R., Calzolari G., Canepari S., Casasanta G., Ciampichetti S., Conidi A., Cordelli E.,
1675 713 Di Ianni A., Di Liberto L., Facchini M. C., Facci A., Frasca D., Gilardnoni S., Grollino M. G., Gualtieri M.,
1676 714 Lucarelli F., Malaguti A., Manigrasso M., Montagnoli M., Nava S., Padoan E., Perrino C., Petralia E.,
1677 715 Petenko I., Querol X., Simonetti G., Tranfo G., Ubertini S., Valli G., Valentini S., Vecchi R., Volpi F.,
1678 716 Weinhold K., Wiedensholer A., Zanini G., Gobbi G. P., 2017. First Results of the “Carbonaceous
1679 717 Aerosol in Rome and Environs (CARE)” Experiment: Beyond Current Standards for PM₁₀. Atmosphere
1680 718 8, 249; doi:10.3390/atmos8120249
1681 719
1682 719 Costabile F., Gualtieri M., Canepari S., Tranfo G., Consales C., Grollino M.G., Paci E., Petralia E., Pignini
1683 720 D., Simonetti G., 2019. Evidence of association between aerosol properties and in-vitro cellular
1684 721 oxidative response to PM₁, oxidative potential of PM_{2.5}, a biomarker of RNA oxidation, and its
1685 722 dependency on the combustion aerosol. Atmospheric Environment 213, 445-455; doi
1686 723 10.1016/j.atmosenv.2019.06.023
1687 724
1688 724 Diapouli E., Manousakas M.I., Vratolis S., Vasilatou V., Pateraki S., Bairachtari K.A., Querol X., Amato
1689 725 F., Alastuey A., Karanasiou A.A., Lucarelli F., Nava S., Calzolari G., Gianelle V.L., Colombi C., Alves C.,
1690 726 Custódio D., Pio C., Spyrou C., Kallos G.B., Eleftheriadis K.; AIRUSE-LIFE+: estimation of natural
1691 727 source contributions to urban ambient air PM₁₀ and PM_{2.5} concentrations in southern Europe –
1692 728
1693 728
1694 728
1695 728
1696 728
1697 728
1698 728
1699 728
1700 728
1701 728
1702 728
1703 728
1704 728
1705 728
1706 728
1707 728
1708 728
1709 728
1710 728
1711 728

1712
1713
1714 729 implications to compliance with limit values; *Atmospheric Chemistry and Physics* 17, 3673–3685,
1715 730 2017; doi:10.5194/acp-17-3673-2017
1716
1717
1718 731 Dockery D.W., Pope C.A., Xu X., Spengler J.D., Ware J.H., Fay M.E., Ferris B.G., Speizer F.E., 1993. An
1719 732 Association between Air Pollution and Mortality in Six U.S. Cities. *The New England Journal of*
1720
1721 733 *Medicine* 329, 1753-1759
1722
1723 734 Donato A., Lo Feudo T., Marinoni A., Dinoi A., Avolio E., Merico E., Calidonna C.R., Contini D.,
1724 735 Bonasoni P.; Characterization of In Situ Aerosol Optical Properties at Three Observatories in the
1725 736 Central Mediterranean; *Atmosphere* 2018, 9, 369; doi:10.3390/atmos9100369
1726
1727
1728 737 Drinovec L., Močnik G., Zotter P., Prévôt A.S.H., Ruckstuhl C., Coz E., Rupakheti M., Sciare J., Müller
1729 738 T., Wiedensohler E., and Hansen D.A., 2015. The “dual-spot” Aethalometer: an improved
1730 739 measurement of aerosol black carbon with real-time loading compensation. *Atmospheric*
1731 740 *Measurement Techniques* 8, 1965-1979; doi:10.5194/amt-8-1965-2015
1732
1733 741 Dubovik O., Holben B., Eck T. F., Smirnov A., Kaufman Y. J., King M. D., Tanré D., Slutsker I., 2002.
1734 742 Variability of Absorption and Optical Properties of Key Aerosol Types Observed in Worldwide
1735 743 Locations. *Journal of the Atmospheric Sciences* 59, 590-608
1736
1737
1738 744 Ealo M., Alastuey A., Ripoll A., Pérez N., Minguillón M.C., Querol X., and Pandolfi M., 2016. Detection
1739 745 of Saharan dust and biomass burning events using near-real-time intensive aerosol optical
1740 746 properties in the north-western Mediterranean. *Atmospheric Chemistry and Physics* 16, 12567–
1741 747 12586; doi:10.5194/acp-16-12567-2016
1742
1743
1744 748 Fialho P., Freitas M.C., Barata F., Vieira B., Hansen A.D.A., Honrath R.E., 2006. The Aethalometer
1745 749 calibration and determination of iron concentration in dust aerosols. *Journal of Aerosol Science* 37,
1746 750 1497 – 1506; doi:10.1016/j.jaerosci.2006.03.002
1747
1748
1749 751 Eck T.F., Holben B.N., Reis J.S., Dubovik O., Smirnov A., O’Neill N.T., Slutsker I., and Kinne S., 1999.
1750 752 Wavelength dependence of the optical depth of biomass burning, urban, and desert dust aerosols.
1751 753 *Journal of Geophysical Research* 104, D24, 31333-31349
1752
1753
1754 754 Giles D.M., Holben B.N., Tripathi S.N., Eck T.F., Newcomb W.N., Slutsker I., Dickerson R.R., Thompson
1755 755 A.M., Mattoo S., Wang S.-H., Singh R.P., Sinyuk A., and Schafer J.S., 2011. Aerosol properties over
1756 756 the Indo-Gangetic Plain: A mesoscale perspective from the TIGERZ experiment. *Journal of*
1757 757 *Geophysical Research* 116, D18203, doi:10.1029/2011JD015809
1758
1759
1760 758 Giles D.M., Holben B.N., Eck T.F., Sinyuk A., Smirnov A., Slutsker I., Dickerson R.R., Thompson A.M.,
1761 759 and Schafer J.S., 2012. An analysis of AERONET aerosol absorption properties and classifications
1762
1763
1764
1765
1766
1767
1768
1769
1770

1771
1772
1773 760 representative of aerosol source regions. Journal of Geophysical Research 117, D17203,
1774 761 doi:10.1029/2012JD018127
1775
1776
1777 762 Goetz J.D., Giordano M.R., Stockwell C.E., Christian T.J., Maharian R., Adhikari S., Bhave P.V., Praveen
1778 763 P.S., Panday A.K., Jayarathne T., Stone E.A., Yokelson R.J., and DeCarlo P.F., 2018. Speciated online
1779 764 PM1 from South Asian combustion sources – Part1: Fuel-based emission factors and size
1780 765 distributions. Atmospheric Chemistry and Physics 18, 14653–14679; [https://doi.org/10.5194/acp-
1781 766 18-14653-2018](https://doi.org/10.5194/acp-18-14653-2018)
1782
1783 767 Gobbi G. P., Kaufman Y. J., Koren I., Eck T. F., 2007. Classification of aerosol properties derived from
1784 768 AERONET direct sun data. Atmospheric Chemistry and Physics, 7, 453–458; [www.atmos-chem-
1785 769 phys.net/7/453/2007/](http://www.atmos-chem-phys.net/7/453/2007/)
1786
1787 770 Gobbi G. P., Barnaba F., Di Liberto L., Bolignano A., Lucarelli F., Nava S., Perrino C., Pietrodangelo A.,
1788 771 Basart S., Costabile F., Dionisi D., Rizza U., Canepari S., Sozzi R., Morelli M., Manigrasso M., Drenwick
1789 772 F., Stuckmeier C., Poenitz K., Wille K., 2019. An inclusive view of Saharan dust advections to Italy and
1790 773 the Central Mediterranean. Atmospheric Environment 2019, 242–256;
1791 774 <https://doi.org/10.1016/j.atmosenv.2019.01.002>
1792 775 Horvath H., Alados Alarboledas A., Olmo Reyes F.J., 2018. Angular Scattering of the Sahara Dust
1793 776 Aerosol. Atmospheric Chemistry and Physics 18, 17735–17744; [https://doi.org/10.5194/acp-18-
1794 777 17735-2018](https://doi.org/10.5194/acp-18-17735-2018)
1795 778 Hyvärinen A.P., Vakkari V., Hooda R.K., Sharma V.P., Panwar T.S., Beukes J.P., van Zyl P.G., Josipovic
1796 779 M., Garland R.M., Andreae M.O., Pöschl U., Petzold A., 2013. Correction for a measurement artifact
1797 780 of the Multi-Angle Absorption Photometer (MAAP) at high black carbon mass concentration levels.
1798 781 Atmospheric Measurement Techniques 6, 81-90; doi:10.5194/amt-6-81-2013
1799 782 IPCC, Climate Change 2013: The Physical Science Basis (Working Group I Contribution to the Fifth
1800 783 Assessment Report of the Intergovernmental Panel on Climate Change - IPCC),
1801 784 <http://www.ipcc.ch/report/ar5/wg1/>
1802 785 Kalapureddy M. C. R., Kaskaoutis D. G., Raj P. E., Devara P. C. S., Kambezidis H. D., Kosmopoulos P.
1803 786 G., Nastos P. T., 2009. Identification of aerosol type over the Arabian Sea in the premonsoon season
1804 787 during the Integrated Campaign for Aerosol, Gases and Radiation Budget (ICARB). Journal of
1805 788 Geophysical Research, Vol. 114, D17203, doi:10.1029/2009JD011826
1806 789 Kaufman, Y. J., 1993. Aerosol optical thickness and atmospheric path radiance. J. Geophys. Res.,
1807 790 98(D2), 2677–2692
1808
1809
1810
1811
1812
1813
1814
1815
1816
1817
1818
1819
1820
1821
1822
1823
1824
1825
1826
1827
1828
1829

1830
1831
1832
1833 791 Khlystov A., Stanier C., Pandis S.N., 2004. An algorithm for combining electrical mobility and
1834 792 aerodynamic size distributions data when measuring ambient aerosol special issue of aerosol
1835
1836 793 science and technology on findings from the fine particulate matter supersites program. Aerosol
1837
1838 794 Science and Technology 38, 229–238; DOI: 10.1080/02786820390229543
1839 795 Lee S., Yoo S.-C., Lim S.-W., Kim Y. P., Ghim Y.S., Kim J.-H., Kang C.-H., Kim Y.J., Chang L.-S., Lee S.-J.,
1840
1841 796 2012. Spectral dependency of light scattering/absorption and hygroscopicity of pollution and dust
1842
1843 797 aerosols in Northeast Asia. Atmospheric Environment 50, 246-254;
1844 798 doi:10.1016/j.atmosenv.2011.12.026
1845
1846 799 Lihavainen H., Alghamdi M.A., Hyvärinen A., Hussein T., Neitola K., Khoder M., Abdelmaksoud A.S.,
1847
1848 800 Al-Jeelani H., Shabbaj I.I., and Almehmadi F.M., 2017. Aerosol optical properties at rural background
1849 801 area in Western Saudi Arabia. Atmospheric Research 197, 370–378;
1850
1851 802 <http://dx.doi.org/10.1016/j.atmosres.2017.07.019>
1852
1853 803 Lucarelli F., Chiari M., Calzolari G., Giannoni M., Nava S., Udisti R., Severi M., Querol X., Amato F.,
1854 804 Alves C., Eleftheriasdis K., 2015. The role of PIXE in the AIRUSE project “testing and development of
1855
1856 805 air quality mitigation measures in Southern Europe”. Nuclear Instruments and Methods in Physics
1857
1858 806 Research B 363, 92–98; <http://dx.doi.org/10.1016/j.nimb.2015.08.023>
1859
1860 807 Moosmüller H., and Chackabarty R.K., 2011. Technical Note: Simple Analytical Relationships
1861 808 between Ångström Coefficients of Aerosol Extinction, Scattering, Absorption, and Single Scattering
1862
1863 809 Albedo. Atmospheric Chemistry and Physics 11, 10677-10680; [https://doi.org/10.5194/acp-11-](https://doi.org/10.5194/acp-11-10677-2011)
1864 810 [10677-2011](https://doi.org/10.5194/acp-11-10677-2011)
1865
1866 811 Müller T., Laborde M., Kassell G., and Wiedensohler A., 2011a. Design and performance of a three-
1867
1868 812 wavelength LED-based total scatter and backscatter integrating nephelometer. Atmospheric
1869
1870 813 Measurement Techniques 4, 1291–1303; doi:10.5194/amt-4-1291-2011
1871 814 Müller T., Henzing J.S., de Leeuw G., Wiedensohler E., Alastuey A., Angelov H., Bizjak M., Collaud
1872
1873 815 Coen M., Engström J.E., Gruening C., Hillamo R., Hoffer A., Imre K., Ivanow P., Jennings G., Sun J.Y.,
1874
1875 816 Kalivitis N., Karlsson H., Komppula M., Laj P., Li S.-M., Lunder C., Marinoni A., Martins dos Santos S.,
1876 817 Moerman M., Nowak A., Ogren J.A., Petzold A., Pichon J.M., Rodriguez S., Sharma S., Sheridan P.J.,
1877
1878 818 Teinilä K., Tuch T., Viana M., Weingartner E., Wilhelm R., and Wang Y.Q., 2011b. Characterization
1879
1880 819 and intercomparison of aerosol absorption photometers: results of two intercomparison
1881
1882 820 workshops. Atmospheric Measurement Techniques 4, 245–268; doi:10.5194/amt-4-245-2011
1883
1884
1885
1886
1887
1888

1889
1890
1891
1892
1893
1894
1895
1896
1897
1898
1899
1900
1901
1902
1903
1904
1905
1906
1907
1908
1909
1910
1911
1912
1913
1914
1915
1916
1917
1918
1919
1920
1921
1922
1923
1924
1925
1926
1927
1928
1929
1930
1931
1932
1933
1934
1935
1936
1937
1938
1939
1940
1941
1942
1943
1944
1945
1946
1947

821 Nava S., Becagli S., Calzolari G., Chiari M., Lucarelli F., Prati P., Traversi R., Udisti R., Valli G., Vecchi
822 R., 2012. Saharan dust impact in central Italy: An overview on three years elemental data records.
823 Atmospheric Environment 60, 444-452; <http://dx.doi.org/10.1016/j.atmosenv.2012.06.064>
824 Ng N.L., Herndon S.C., Trimborn A., Canagaratna M.R., Croteau P., Onasch T.M., Sueper D., Worsnop
825 D.R., Zhang Q., Sun Y.L., and Jayne J.T., 2011. An Aerosol Chemical Speciation Monitor (ACSM) for
826 routine monitoring of atmospheric aerosol composition. Aerosol Science and Technology 45, 770-
827 784; DOI: 10.1080/02786826.2011.560211
828 Perrino C., Canepari S., Catrambone M., Dalla Torre S., Rantica E., Sargolini T., 2009. Influence of
829 natural events on the concentration and composition of atmospheric particulate matter.
830 Atmospheric Environment 43, 4766-4779; doi:10.1016/j.atmosenv.2008.06.035
831 Pope III C.A., Burnett R.T., Thun M.J., Calle E.E., Krewski D., Ito K., Thurston G.D., 2002. Lung Cancer,
832 Cardiopulmonary Mortality, and Long-term Exposure to Fine Particulate Air Pollution. Journal of the
833 American Medical Association 287, 1132-1141
834 Querol X., Pérez N., Reche C., Ealo M., Ripoll A., Tur J., Pandolfi M., Pey J., Salvador P., Moreno T.,
835 Alastuey A., 2019; African dust and air quality over Spain: Is it only dust that matters?; Science of
836 the Total Environment 686, 737-752;
837 <https://doi.org/10.1016/j.scitotenv.2019.05.349>
838 Ramachandran S, 2018. Atmospheric Aerosols -
839 Characteristics and Radiative Effects. Taylor and Francis; ISBN 1498750737
840 Romano S., Perrone M.R., Pavese G., Esposito F., Calvello M., 2019. Optical properties of PM2.5
841 particles: Results from a monitoring campaign in southeastern Italy. Atmospheric Environment 203,
842 35-47; <https://doi.org/10.1016/j.atmosenv.2019.01.037>
843 Rupakheti D., Kang S., Bilal M., Gong J., Xia X., Cong Z., 2019. Aerosol optical depth climatology over
844 Central Asian countries based on Aqua-MODIS Collection 6.1 data: Aerosol variations and sources.
845 Atmospheric Environment 207, 205-214; <https://doi.org/10.1016/j.atmosenv.2019.03.020>
846 Russell P. B., Bergstrom R. W., Shinozuka Y., Clarke A. D., DeCarlo P. F., Jimenez J. L., Livingston J.
847 M., Redemann J., Dubovik O., Strawa A., 2010. Absorption Angstrom Exponent in AERONET and
848 related data as an indicator of aerosol composition. Atmospheric Chemistry and Physics 10, 1155-
849 1169; www.atmos-chem-phys.net/10/1155/2010/
850 Sandradewi J., Prévôt A.S.H., Szidat S., Perron N., Alfarra M.R., Lanz V.A., Weingartner E., and
851 Baltensperger U., 2008. Using Aerosol Light Absorption Measurements for the Quantitative

1948
1949
1950 851 Determination of Wood Burning and Traffic Emission Contributions to Particulate Matter. Environ.
1951
1952 852 Sci. Technol. 42, 3316–3323
1953
1954 853 Schmeisser L., Andrews E., Ogren J.A., Sheridan P., Jefferson A., Sharma S., Kim J.E., Sherman J.P.,
1955
1956 854 Sorribas M., Kalapov I., Arsov T., Angelov C., Mayol-Bracero O.M., Labuschagne C., Kim S.-W., Hoffer
1957 855 A., Lin N.-H., Chia H.-P., Bergin M., Sun J., Liu P., and Wu H., 2017. Classifying aerosol type using in
1958
1959 856 situ surface spectral aerosol optical properties. Atmospheric Chemistry and Physics 17, 12097–
1960
1961 857 12120; <https://doi.org/10.5194/acp-17-12097-2017>
1962 858 Schuster G.L., Dubovik O., and Holben B.N., 2006. Angstrom exponent and bimodal aerosol size
1963
1964 859 distributions. Journal of Geophysical Research 111, D07207, doi:10.1029/2005JD006328
1965
1966 860 Segura S., Estellés V., Titos G., Lyamani H., Utrillas M.P., Zotter P., Prévôt A.S.H., Močnik G., Alados-
1967 861 Alarboledas L., and Martínez-Lozano J.A., 2014. Determination and analysis of in situ spectral
1968
1969 862 aerosol optical properties by a multi-instrumental approach. Atmospheric Measurement
1970
1971 863 Techniques 7, 2373–2387; doi:10.5194/amt-7-2373-2014
1972
1973 864 Seinfeld J.H., Pandis S., 1998. Atmospheric Chemistry and Physics. From Air Pollution to Climate
1974 865 Change. Wiley-Interscience
1975
1976 866 Takemura T., Nakajima T., Dubovik O., Holben B.N., Kinne S., 2002. Single-Scattering Albedo and
1977 867 Radiative Forcing of Various Aerosol Species with a Global Three-Dimensional Model. Journal of
1978
1979 868 Climate 15(4)
1980
1981 869 Timonen H., Aurela M., Carbone S., Saarnio K., Saarikoski S., Mäkelä T., Kulmala M., Kerminen V.-
1982
1983 870 M., Worsnop D.R., and Hillamo R., 2010. High time-resolution chemical characterization of the
1984
1985 871 water-soluble fraction of ambient aerosols with PILS-TOC-IC and AMS. Atmospheric Measurement
1986 872 Techniques 3, 1063–1074; doi:10.5194/amt-3-1063-2010
1987
1988 873 Titos G., Ealo M., Pandolfi M., Pérez N., Sola Y., Sicard M., Comerón A., Querol X., and Alastuey A.,
1989
1990 874 2017. Spatiotemporal evolution of a severe winter dust event in the western Mediterranean:
1991 875 Aerosol optical and physical properties. J. Geophys. Res. Atmos., 122, 4052–4069,
1992
1993 876 doi:10.1002/2016JD026252
1994
1995 877 Valenzuela A., Olmo F.J., Lyamani H., Antón M., Titos G., Cazorla A., Alados-Alarboledas L., 2015.
1996 878 Aerosol scattering and absorption Angström exponents as indicators of dust and dust-free days over
1997
1998 879 Granada (Spain). Atmospheric Research 154, 1–13;
1999 880 <http://dx.doi.org/10.1016/j.atmosres.2014.10.015>
2000
2001
2002
2003
2004
2005
2006

2007
2008
2009
2010
2011
2012
2013
2014
2015
2016
2017
2018
2019
2020
2021
2022
2023
2024
2025
2026
2027
2028
2029
2030
2031
2032
2033
2034
2035
2036
2037
2038
2039
2040
2041
2042
2043
2044
2045
2046
2047
2048
2049
2050
2051
2052
2053
2054
2055
2056
2057
2058
2059
2060
2061
2062
2063
2064
2065

881 Viana M., Amato F., Alastuey A., Querol X., Moreno T., García Dos Santos S., Herce M.D., and
882 Fernández-Patier R., 2009. Chemical Tracers of Particulate Emissions from Commercial Shipping.
883 Environ. Sci. Technol. 43, 7472–7477; <https://doi.org/10.1021/es901558t>
884 Yang M., Howell S.G., Zhuang J., and Huebert B.J., 2009. Attribution of aerosol light absorption to
885 black carbon, brown carbon, and dust in China – interpretations of atmospheric measurements
886 during EAST-AIRE. Atmospheric Chemistry and Physics 9, 2035–2050; [www.atmos-chem-](http://www.atmos-chem-phys.net/9/2035/2009/)
887 [phys.net/9/2035/2009/](http://www.atmos-chem-phys.net/9/2035/2009/)
888 Zotter P., Herich H., Gysel M., El-Haddad I., Zhang Y., Močnik G., Hüglin C., Baltensperger U., Szidat
889 S., and Prévôt A.S.H., 2017. Evaluation of the absorption Ångström exponents for traffic and wood
890 burning in the Aethalometer-based source apportionment using radiocarbon measurements of
891 ambient aerosol. Atmospheric Chemistry and Physics 17, 4229–4249Re; doi:10.5194/acp-17-4229-
892 2017

Declaration of interests

The authors declare that they have no known competing financial interests or personal relationships that could have appeared to influence the work reported in this paper.

The authors declare the following financial interests/personal relationships which may be considered as potential competing interests:

SUPPLEMENTARY MATERIAL

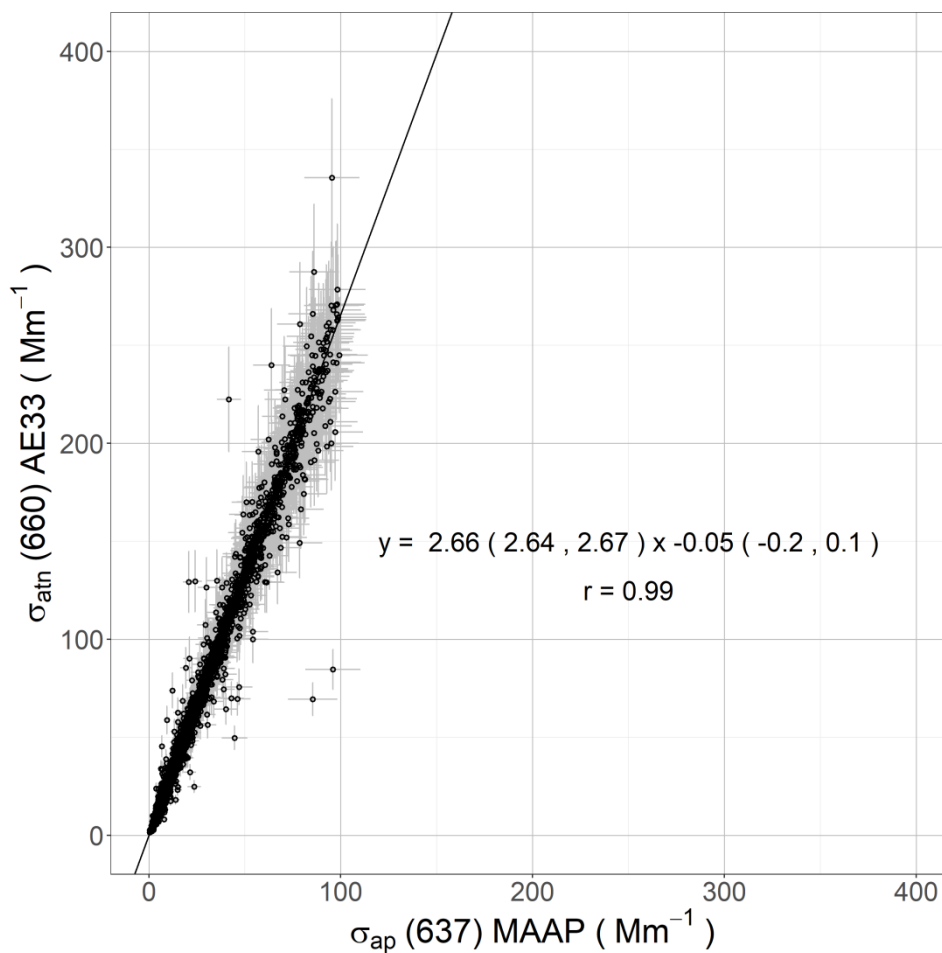


Figure S1 Linear regression analysis performed to determine the factor C_{corr} used to correct AE33 data; numbers in brackets are 95% confidence intervals of regression parameters.

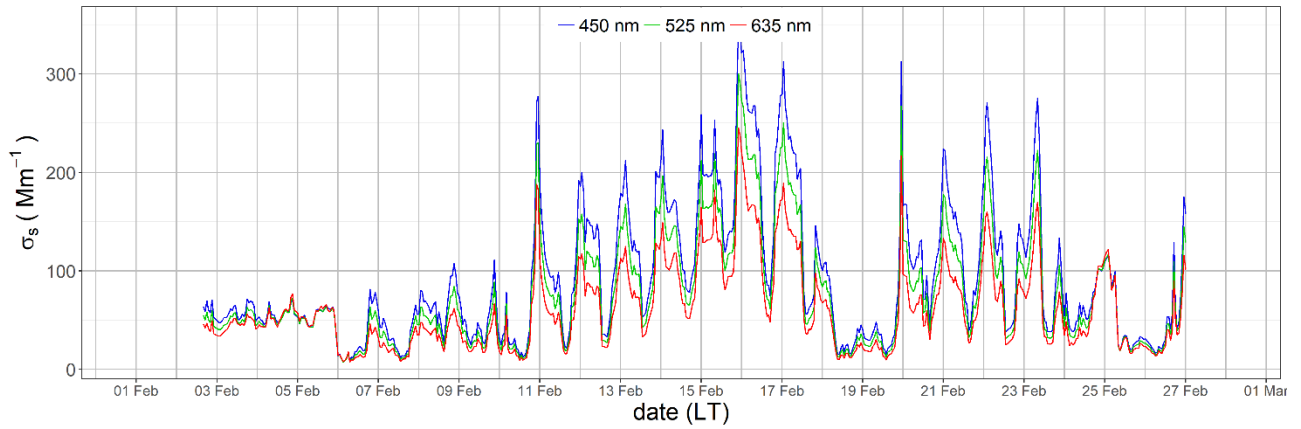


Figure S2 Temporal pattern of multi-wavelength scattering coefficient during the CARE campaign.

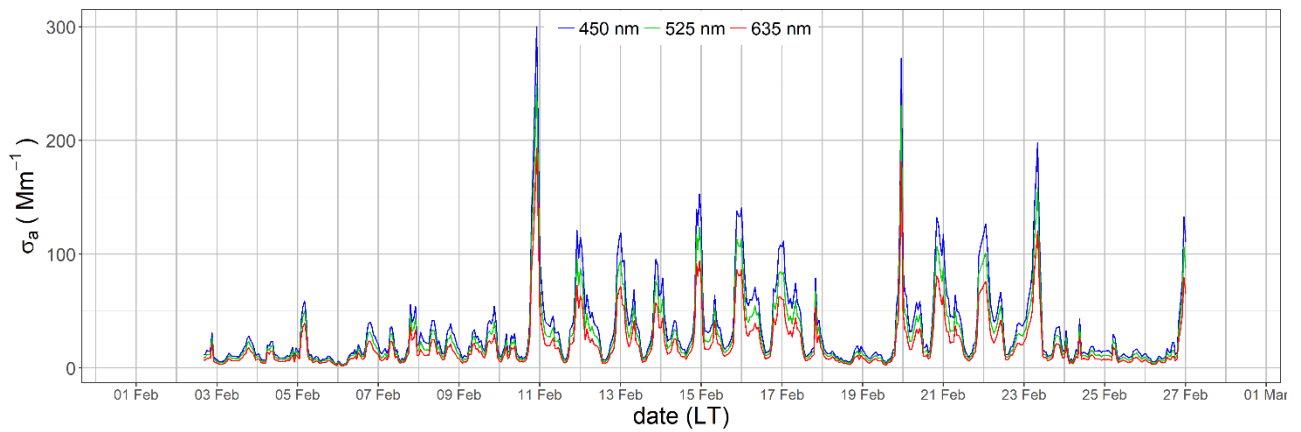


Figure S3 Temporal pattern of multi-wavelength absorption coefficient during the CARE campaign.

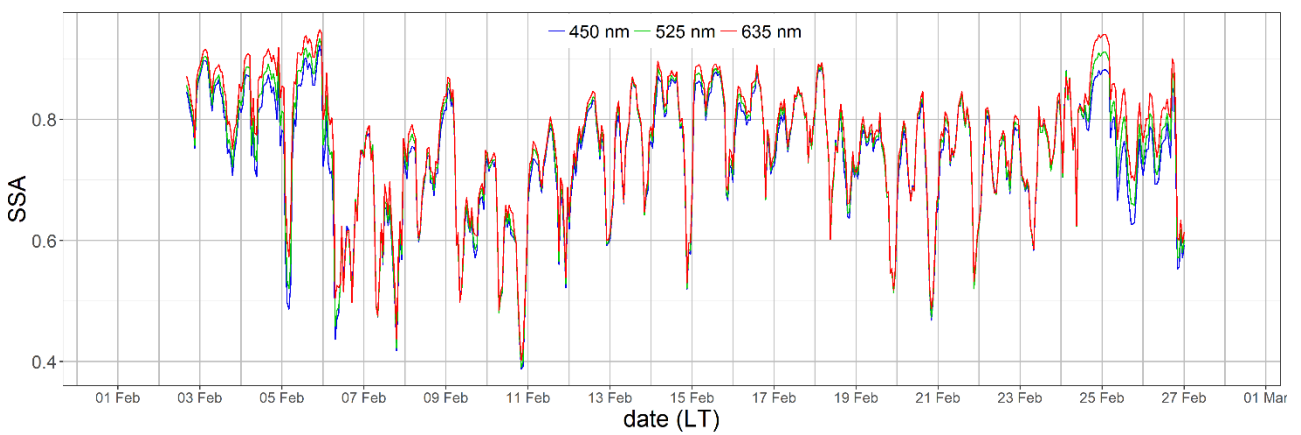


Figure S4 Temporal pattern of multi-wavelength single scattering albedo during the CARE campaign.

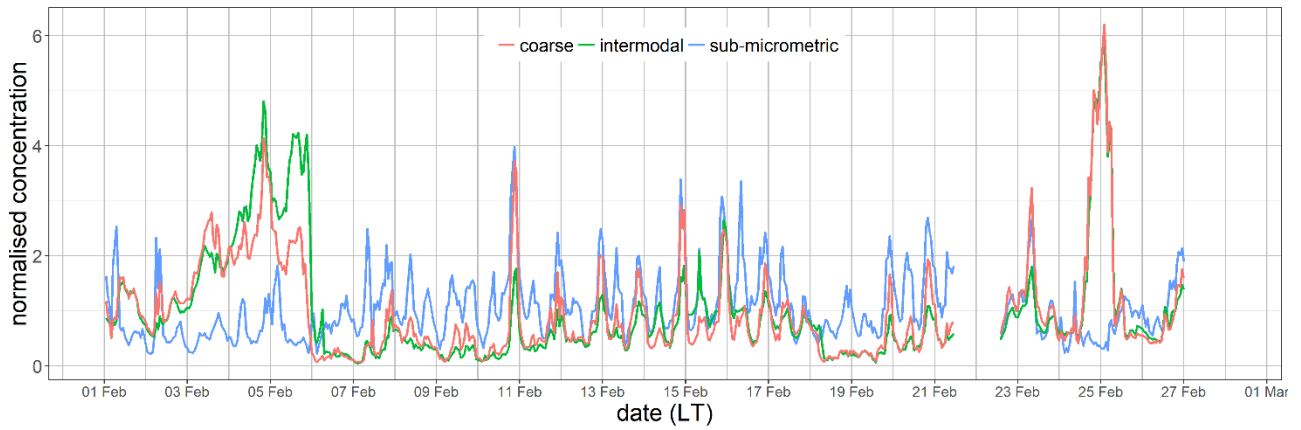


Figure S5 Temporal pattern of particle number concentration in sub-micrometric, intermodal and coarse size fractions during the CARE campaign. concentrations are normalised to the average value of each fraction during the experiment.

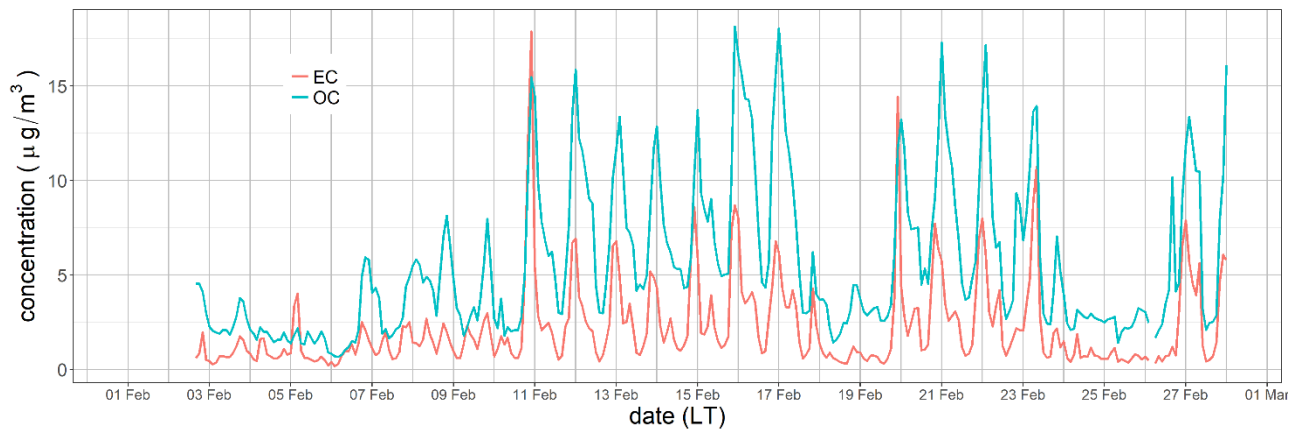


Figure S6 Temporal pattern of EC and OC concentration during the CARE campaign.

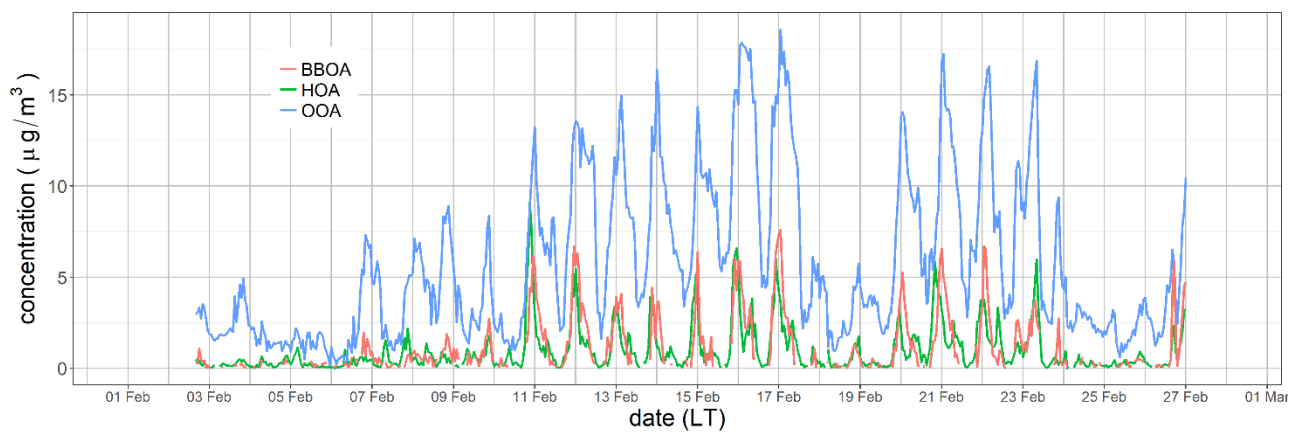


Figure S7 Temporal pattern of BBOA, HOA, and OOA concentrations during the CARE campaign.

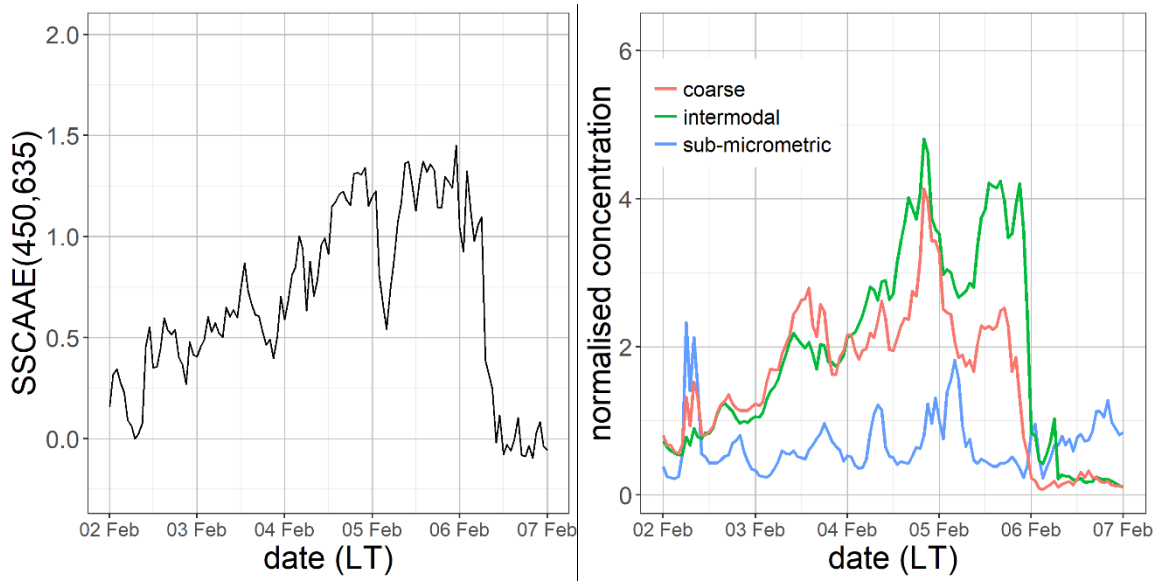


Figure S8 Temporal patterns of SSAE(450,635) (left) and size-segregated particle number concentration normalised on the campaign average (right) during the sea salt aerosol advection episode.

NOAA HYSPLIT MODEL
 Backward trajectories ending at 1900 UTC 04 Feb 17
 GDAS Meteorological Data

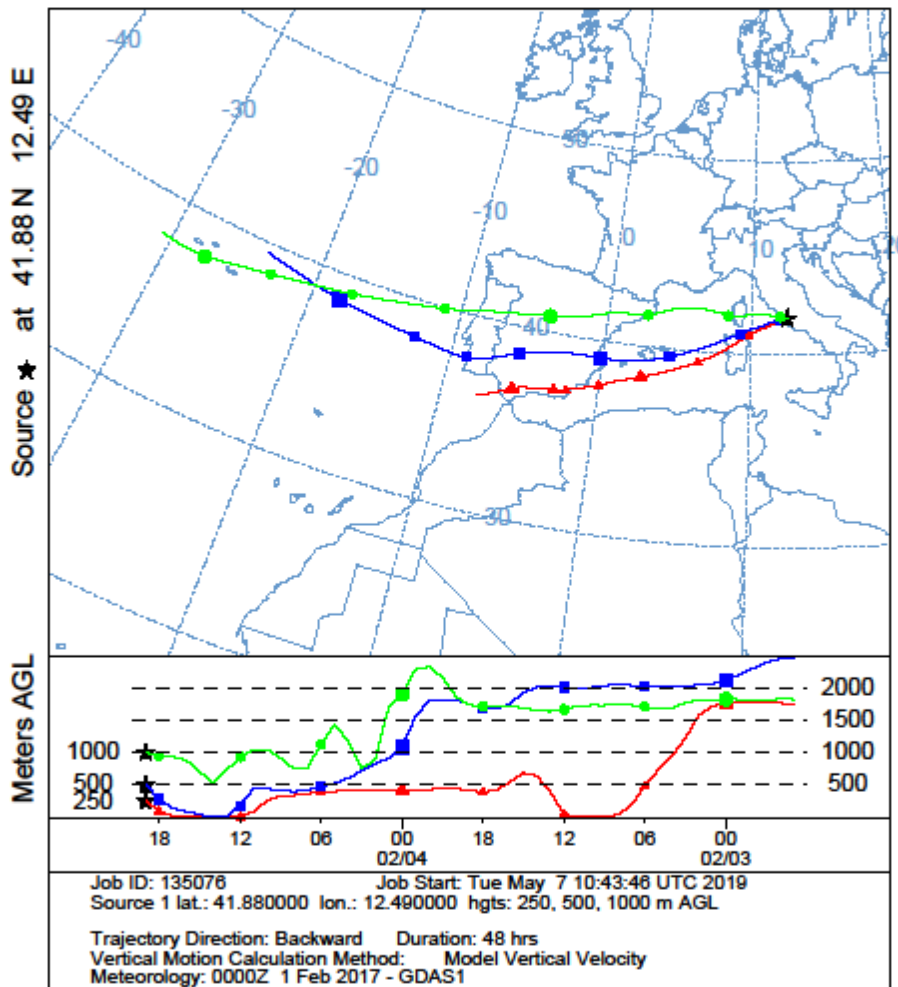


Figure S9 Back trajectory analysis related to the sea salt aerosol advection.

NOAA HYSPLIT MODEL
 Backward trajectories ending at 1900 UTC 24 Feb 17
 GDAS Meteorological Data

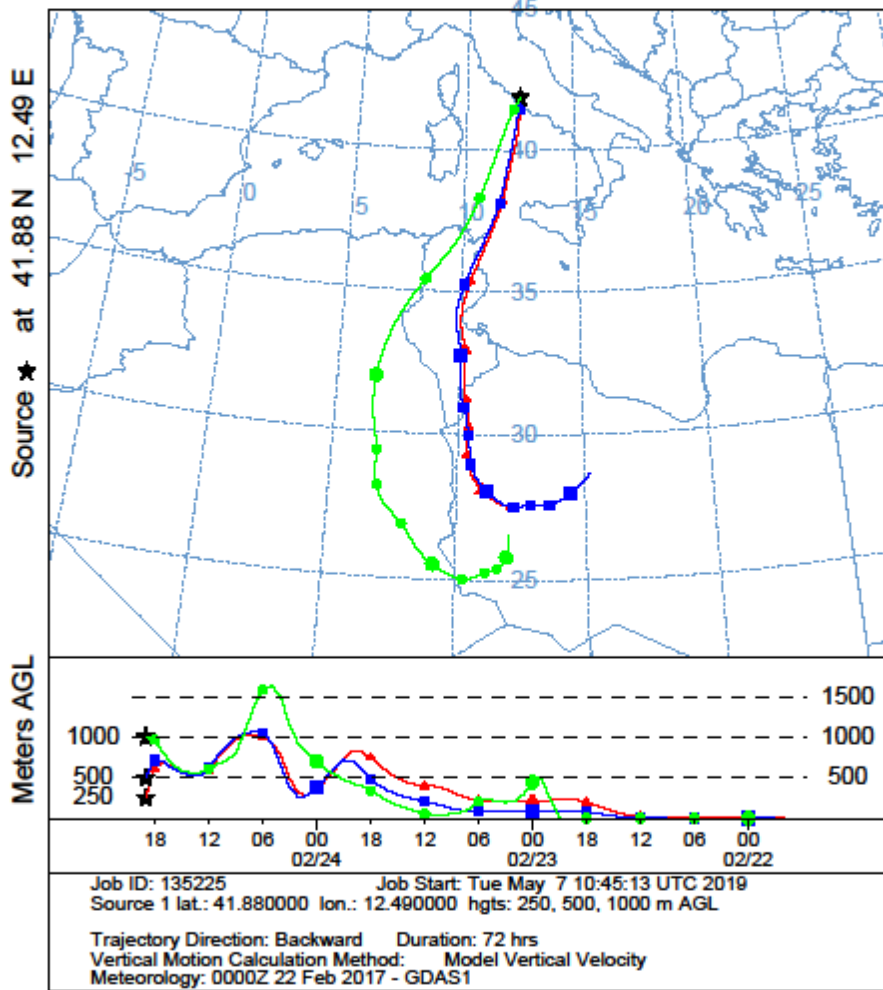


Figure S10 Back trajectory analysis related to the Saharan dust advection.

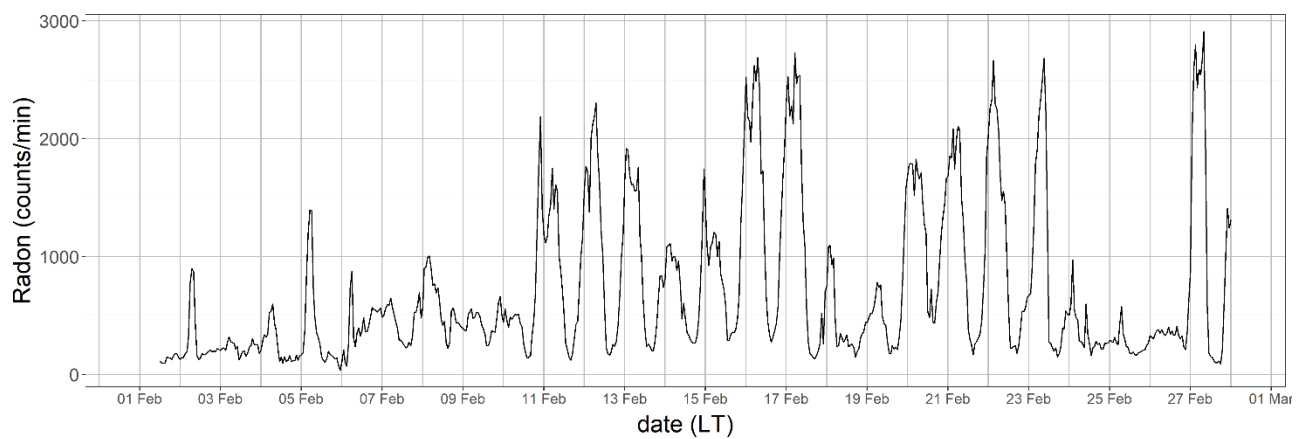


Figure S11 Temporal pattern of ^{222}Rn concentration during the CARE campaign.